People`s Democratic Republic of Algeria

Ministry of Higher Education and Scientific Research

University of Echahid Hamma Lakhdar – El Oued

Faculty of Technology

Dissertation

ACADEMIC MASTER

Domain: Science and Technology

Specialty: Chemical Engineering

Presented by:

1. chaima alia

Entitled:

Plasma-engineered defects in TiO_2/g-C_3N_4 heterojunctions for enhanced charge transfer and solar hydrogen evolution

Publicly defended in : 14/06 /2026

Board of Examiners:

Dr. Lakhdar Sak	**Chairman**
Dr. Wahida Dia	**Examiner**
Dr. Abdelatif Aouadi Université Paris-Saclay	**Supervisor**
Dr. Nader Shehata Kuwait College of Science and Technology	**Supervisor**
Dr. Salah Eddine Laouini University of Echahid Hamma Lakhdar - El Oued	**Supervisor**

Academic Year : 2025/2026

Dedication

The beauty of endings is tied to their beginnings
And the rose only blooms in the goodness of its environment.
My family
♥

And if the sun shines, do not forget
The moon that gave its light so it could shine.
My mother
♥

I gift you a success that you yourselves gifted to me
For a woman never lets down those who stayed awake to support her.
My father
♥

Oh companion, you were a light upon my path
How desolate is a road without your footsteps.
Hanane
♥

And my gratitude, from which I exclude no one
And my love, which encompasses the entire universe with its galaxy.
♥

Gratitude & Appreciation

﴿ لَئِن شَكَرْتُمْ لَأَزِيدَنَّكُمْ ﴾

All praise is due to Allah, abundant, pure, and blessed praise, who has granted us success and enabled us to complete this humble work. To Him, Glorified and Exalted be He, belongs all gratitude and thanks for His blessings, which are countless and beyond enumeration.

I extend my sincere gratitude and profound appreciation to my supervisor, Dr. **Aouadi Abdelatif**, for his invaluable supervision, sound guidance, patience, and unwavering support throughout the period of preparing this thesis. He was truly the best source of support for me. May Allah reward him with the best of rewards on my behalf.

I also extend my heartfelt thanks and high esteem to the co-supervisors, Dr. **Laouini Salah Eddine** and Dr. **Shehata Nader**, as well as to the Dean of the college, for the support, guidance, and valuable advice they provided, which greatly contributed to the completion of this work.

Furthermore, I offer my sincere gratitude and appreciation to all our esteemed professors, under whom we had the privilege of learning throughout our academic journey, for the knowledge, wisdom, and invaluable guidance they imparted, which have significantly shaped our academic and intellectual development.

Finally, I thank everyone who contributed, whether directly or indirectly, to the completion of this modest work.

Abstract:

Hydrogen production from solar energy is considered one of the most promising solutions for addressing the global energy crisis and achieving sustainable energy systems. However, the practical efficiency of semiconductor photocatalysts is still limited by poor visible-light utilization and rapid recombination of photogenerated charge carriers. In this work, a defect-engineered TiO_2/g-C_3N_4 heterojunction photocatalyst was developed by integrating plasma-induced defect engineering with heterostructure construction. TiO_2 nanoparticles were synthesized via a green dual bio-combustion method using citrus peel biomass, while g-C_3N_4 was modified through hydrogen plasma treatment to introduce defect states and tailor its electronic structure.

Structural and optical characterizations confirmed that plasma treatment enhances visible-light absorption, increases surface area, and introduces defect sites that promote charge separation. Among the prepared samples, the optimized 40TiO_2/d-g-C_3N_4 composite exhibited the best photocatalytic performance with a hydrogen evolution rate of 8.9 mmol g^{-1} h^{-1} under simulated solar irradiation, which is higher than most previously reported TiO_2/g-C_3N_4 systems. Photoelectrochemical analysis revealed significantly improved photocurrent responses, indicating efficient interfacial charge transfer within the heterojunction. The enhanced activity is attributed to the synergistic effect between plasma-induced defect states and the TiO_2/g-C_3N_4 heterojunction, which facilitates charge separation and suppresses electron–hole recombination. In addition, the optimized photocatalyst demonstrated excellent stability with minimal activity loss after repeated cycles.

This study provides an effective strategy for designing high-performance photocatalysts by combining defect engineering, heterojunction construction, and green synthesis, offering promising prospects for sustainable solar hydrogen production.

Résumé :

La production d'hydrogène à partir de l'énergie solaire est considérée comme l'une des solutions les plus prometteuses pour faire face à la crise énergétique mondiale et pour parvenir à des systèmes énergétiques durables. Cependant, l'efficacité pratique des photocatalyseurs semi-conducteurs reste limitée par une faible utilisation de la lumière visible et une recombinaison rapide des porteurs de charge photogénérés. Dans ce travail, un photocatalyseur à hétérojonction TiO_2/g-C_3N_4 modifié par ingénierie des défauts a été développé en combinant une ingénierie des défauts induite par plasma avec la construction d'hétérostructures. Des nanoparticules de TiO_2 ont été synthétisées par une méthode verte de double bio-combustion utilisant de la biomasse d'écorces d'agrumes, tandis que le g-C_3N_4 a été modifié par un traitement au plasma d'hydrogène afin d'introduire des états de défauts et d'ajuster sa structure électronique.

Les caractérisations structurales et optiques ont confirmé que le traitement au plasma améliore l'absorption de la lumière visible, augmente la surface spécifique et introduit des sites de défauts favorisant la séparation des charges. Parmi les échantillons préparés, le composite optimisé 40TiO_2/d-g-C_3N_4 a présenté la meilleure performance photocatalytique avec un taux d'évolution d'hydrogène de 8,9 mmol g^{-1} h^{-1} sous irradiation solaire simulée, ce qui est supérieur à la plupart des systèmes TiO_2/g-C_3N_4 rapportés précédemment. Les analyses photoélectrochimiques ont révélé des réponses de photocourant significativement améliorées, indiquant un transfert de charge interfacial efficace au sein de l'hétérojonction. L'activité accrue est attribuée à l'effet synergique entre les états de défauts induits par plasma et l'hétérojonction TiO_2/g-C_3N_4, qui facilite la séparation des charges et supprime la recombinaison électron-trou. De plus, le photocatalyseur optimisé a démontré une excellente stabilité avec une perte d'activité minimale après des cycles répétés.

Cette étude fournit une stratégie efficace pour concevoir des photocatalyseurs haute performance en combinant l'ingénierie des défauts, la construction d'hétérojonctions et la

الملخص :

يُعتبر إنتاج الهيدروجين من الطاقة الشمسية أحد الحلول الواعدة لمواجهة أزمة الطاقة العالمية وتحقيق أنظمة طاقة مستدامة. ومع ذلك، لا زال الكفاءة العملية للمحفزات الضوئية شبه الموصلة محدودة بسبب ضعف الاستفادة من الضوء المرئي وسرعة إعادة اتحاد حاملات الشحنة المتولدة ضوئيًا. في هذا العمل، تم تطوير محفز ضوئي من نوع الزلوجة غير المتجانسة $TiO_2/g-C_3N_4$ معدّل هندسيًا بالعيوب، من خلال دمج هندسة العيوب المستحثة بالبلازما مع بناء البنية غير المتجانسة. تم تصنيع جسيمات TiO_2 النانوية بطريقة خضراء مزدوجة للاحتراق الحيوي باستخدام كتلة حيوية من قشور الحمضيات، بينما تم تعديل $g-C_3N_4$ بمعالجة ببلازما الهيدروجين لإدخال حالات العيوب وضبط بنيته الإلكترونية.

أكدت الفحوصات البنيوية والبصرية أن معالجة البلازما تعزز امتصاص الضوء المرئي، وتزيد المساحة السطحية، وتُدخل مواقع عيوب تعزز فصل الشحنات. من بين العينات المحضرة، أظهر المتراكب المحسَّن $TiO_2/d-g-40$ C_3N_4 أفضل أداء تحفيزي ضوئي بمعدل إنتاج هيدروجين بلغ 8.9 مليمول جرام$^{-1}$ ساعة$^{-1}$ تحت إشعاع شمسي محاكٍ، وهو أعلى من معظم أنظمة $TiO_2/g-C_3N_4$ المبلغ عنها سابقًا. كشفت التحليلات الكهروضوئية الكيميائية عن استجابات تيار ضوئي محسَّنة بشكل ملحوظ، مما يشير إلى نقل شحنة واجهي فعال داخل الزلوجة غير المتجانسة. يُعزى النشاط المحسَّن إلى التأثير التآزري بين حالات العيوب المستحثة بالبلازما والزلوجة غير المتجانسة $TiO_2/g-C_3N_4$ ، مما يسهل فصل الشحنات ويمنع إعادة اتحاد الإلكترونات والثقوب. بالإضافة إلى ذلك، أظهر المحفز الضوئي المحسَّن ثباتية ممتازة مع فقدان ضئيل في النشاط بعد دورات متكررة.

Keywords :

Green Hydrogen, Photo catalysis, Titanium Dioxide (TiO_2) , Graphitic Carbon Nitride ($g\text{-}C_3N_4$)

Mots-clés :

Hydrogène vert, Photocatalyse, Dioxyde de titane (TiO_2), Nitrure de carbone graphitique

الكلمات المفتاحية:

الهيدروجين الأخضر، الحفز الضوئي، ثاني أكسيد التيتانيوم (TiO_2)، نيتريد الكربون الجرافيتي ($g\text{-}C_3N_4$).

Table of Contents

TABLE OF CONTENTS

Lits of Equatins:

List Of Tables:

list of abbreviations :

Abbreviation	Full Meaning
BET	Brunauer–Emmett–Teller
BJH	Barrett–Joyner–Halenda
CB	Conduction Band
CCUS	Carbon Capture Utilization and Storage
CO_2	Carbon Dioxide
DFT	Density Functional Theory
DRS	Diffuse Reflectance Spectroscopy
EDS	Energy Dispersive Spectroscopy
EDX	Energy Dispersive X-ray Spectroscopy
FTIR	Fourier Transform Infrared Spectroscopy
FTO	Fluorine-doped Tin Oxide
GC-TCD	Gas Chromatography–Thermal Conductivity Detector
g-C_3N_4	Graphitic Carbon Nitride
H_2	Hydrogen
H_2S	Hydrogen Sulfide
PEM	Proton Exchange Membrane
ROS	Reactive Oxygen Species
SEM	Scanning Electron Microscopy
SOEC	Solid Oxide Electrolysis Cell
TEOA	Triethanolamine
TEM	Transmission Electron Microscopy
TiO_2	Titanium Dioxide
TTIP	Titanium Tetraisopropoxide
UV-Vis	Ultraviolet–Visible Spectroscopy
VB	Valence Band
XRD	X-Ray Diffraction
d-g-C_3N_4	Defect-engineered Graphitic Carbon Nitride
mmol	Millimole
g^{-1}	Per Gram
h^{-1}	Per Hour

List Of Figures:

General Introduction

General Introduction:

The increasing global demand for sustainable energy together with the environmental challenges associated with fossil fuel consumption has stimulated extensive research into renewable energy technologies. Hydrogen has been widely recognized as a promising clean energy carrier owing to its high energy density and environmentally benign combustion products [1]. Among the various strategies for hydrogen production, photocatalytic water splitting driven by solar energy has attracted significant attention as a sustainable approach for converting solar energy into chemical fuels [2]. Since the pioneering work demonstrating photoelectrochemical water splitting on TiO_2 electrodes, semiconductor photocatalysis has become an important research field in solar hydrogen production [3].

Among the various semiconductor photocatalysts investigated for solar-driven hydrogen production, titanium dioxide (TiO_2) has been extensively studied owing to its excellent chemical stability, strong oxidation ability, low toxicity, and relatively low cost [4]. However, the practical application of TiO_2 is significantly limited by its wide band gap (~3.2 eV), which restricts light absorption mainly to the ultraviolet region that represents only a small fraction of the solar spectrum [5]. In addition, the rapid recombination of photogenerated electron–hole pairs further suppress its photocatalytic efficiency. Therefore, considerable efforts have been devoted to modifying TiO_2-based photocatalysts through strategies such as doping, nanostructuring, and heterojunction construction in order to enhance visible-light utilization and improve charge separation efficiency [6,7].

Among the various materials explored for coupling with TiO_2, graphitic carbon nitride (g-C_3N_4) has emerged as a promising metal-free photocatalyst due to its suitable band gap (~2.7 eV), visible-light responsiveness, high chemical stability, and facile synthesis from nitrogen-rich precursors [8]. Since the first report of visible-light-driven hydrogen evolution using polymeric graphitic carbon nitride, g-C_3N_4 has attracted considerable attention for photocatalytic applications including hydrogen production, CO_2 reduction, and environmental remediation [9]. Nevertheless, pristine g-C_3N_4 still suffers from several intrinsic limitations, including low electrical conductivity, limited active sites, and rapid recombination of photogenerated charge carriers, which significantly restrict its photocatalytic performance [10].

To address the limitations of both TiO_2 and g-C_3N_4, constructing TiO_2/g-C_3N_4 heterojunction photocatalysts has been widely recognized as an effective strategy to enhance photocatalytic activity by promoting interfacial charge transfer and suppressing electron–hole recombination [11]. Several studies have demonstrated that rationally designed TiO_2/g-C_3N_4 heterostructures can significantly improve photocatalytic hydrogen evolution compared with the individual components. For instance, Zhao et al. reported porous g-C_3N_4/TiO_2 nanotube heterostructures exhibiting enhanced hydrogen evolution performance due to improved charge separation [12]. Similarly, Jiang et al. developed TiO_2 nanodots/g-C_3N_4 heterostructures with improved photocatalytic performance attributed to strong interfacial coupling between the two semiconductors [13]. Despite these advances, the photocatalytic efficiency of TiO_2/g-C_3N_4 systems remains limited by insufficient active sites and inefficient charge transport pathways [14].

THEORETICAL PART

CHAPTER ONE: SEMICONDUCTORS AND THEIR APPLICATIONS

I- 1.Introduction:

Semiconductors are among the most important materials that have garnered wide attention in the fields of scientific research and modern environmental applications, especially in the field of photocatalysis and pollutant treatment. This is due to their ability to interact with light radiation and convert light energy into chemical energy, which is used to break down harmful compounds and produce useful materials [15,16]. In photocatalysis, when a photon with energy equal to or greater than the band gap hits the semiconductor surface, an electron is excited from the valence band to the conduction band, leaving a positive hole. This electron-hole pair (exciton) can initiate reduction and oxidation reactions on the surface, generating highly reactive species such as hydroxyl radicals (•OH) and superoxide anions ($\bullet O_2^-$), which are responsible for degrading pollutants or producing hydrogen [17,18]. Among these materials, both g-C_3N_4 (graphitic carbon nitride) and titanium dioxide (TiO_2) stand out due to their exceptional physical and chemical properties and high stability [19,20]. g-C_3N_4 is characterized by its ability to absorb visible light (band gap ~2.7 eV), making it suitable for solar energy-based applications [19,21], while TiO_2 is known for its high catalytic activity and chemical stability, especially under ultraviolet light (band gap ~3.2 eV for anatase) [15,16]. Therefore, each is used separately or combined together to improve the efficiency of environmental processes, particularly in water treatment and the removal of organic pollutants [22].

I-2. Compound g-C_3N_4:

I-2.1. Definition:

g-C_3N_4 is known as a semiconductor polymer primarily composed of carbon and nitrogen elements, characterized by high chemical and thermal stability [19,23]. Its structure is based on heptazine units (C_6N_7) linked by bridging nitrogen atoms, forming a two-dimensional layered network similar to graphene but with periodic vacancies [24,25,26]. It contains active functional groups such as (--NH and --NH_2) on the edges of the layers, which play an important role in enhancing its catalytic activity. It is also considered one of the electron-rich conjugated polymers, possessing an energy gap of approximately 2.7 electron volts, which grants it the ability to absorb visible light (up to 460 nm) and utilize it in photoreactions [21,27,28]. It is classified among the most important non-metallic materials in the field of photocatalysis, due to its efficiency in removing pollutants and its potential use in hydrogen production, in addition to its low cost and

ease of preparation [19,22]. Compared to TiO_2, g-C_3N_4 utilizes about 43% of the solar spectrum (visible light), whereas TiO_2 only utilizes UV light (less than 5% of the solar spectrum) [19][24].

I- 2.2. His history:

The study of carbon nitride compounds has a long history dating back to the 19th century. In 1834, the compound known as melon was prepared, representing the first known form of this material family [29]. Later, in 1922, research on these materials was expanded, and scientists began exploring the possibility of developing them into more stable forms [29]. A major theoretical advancement came in 1989, when Liu and Cohen predicted the existence of solid phases of C_3N_4 possessing distinctive properties. This prediction sparked significant interest in the scientific community [30]. A true breakthrough occurred in 2009, when Wang and colleagues successfully synthesized g-C_3N_4 that is photocatalytically active under visible light. They achieved this via thermal polymerization of urea or melamine [24][26]. Since this landmark discovery, extensive research has focused on various strategies---including doping, composite formation, and nanostructuring---to further enhance its performance [31,32].

I- 2.3. Structural characteristics:

The compound g-C_3N_4 exhibits several distinctive structural characteristics. It possesses a two-dimensional layered structure similar to that of graphite, formed by interconnected units of carbon and nitrogen atoms. These layers are stacked with an interlayer distance of approximately 0.326 nm, as reported in references [19] and [22]. Furthermore, the material contains active functional groups, including both primary amine (-NH_2) and secondary amine (-NH) groups. These groups play an important role in enhancing its catalytic activity by providing active sites for surface reactions [19,23]. In terms of stability, g-C_3N_4 demonstrates high thermal stability, remaining stable up to 600°C in air, and exhibits strong chemical resistance to most acids, bases, and organic solvents. However, the typical surface area of bulk g-C_3N_4 prepared by direct thermal polymerization is relatively low, ranging from 10 to 50 m^2/g. This surface area can be significantly increased to over 200 m^2/g through exfoliation or nanocasting techniques [19,33]. Additionally, g-C_3N_4 shows photoluminescence in the blue region of the spectrum, a property that makes it useful for optical sensing applications [34,35].

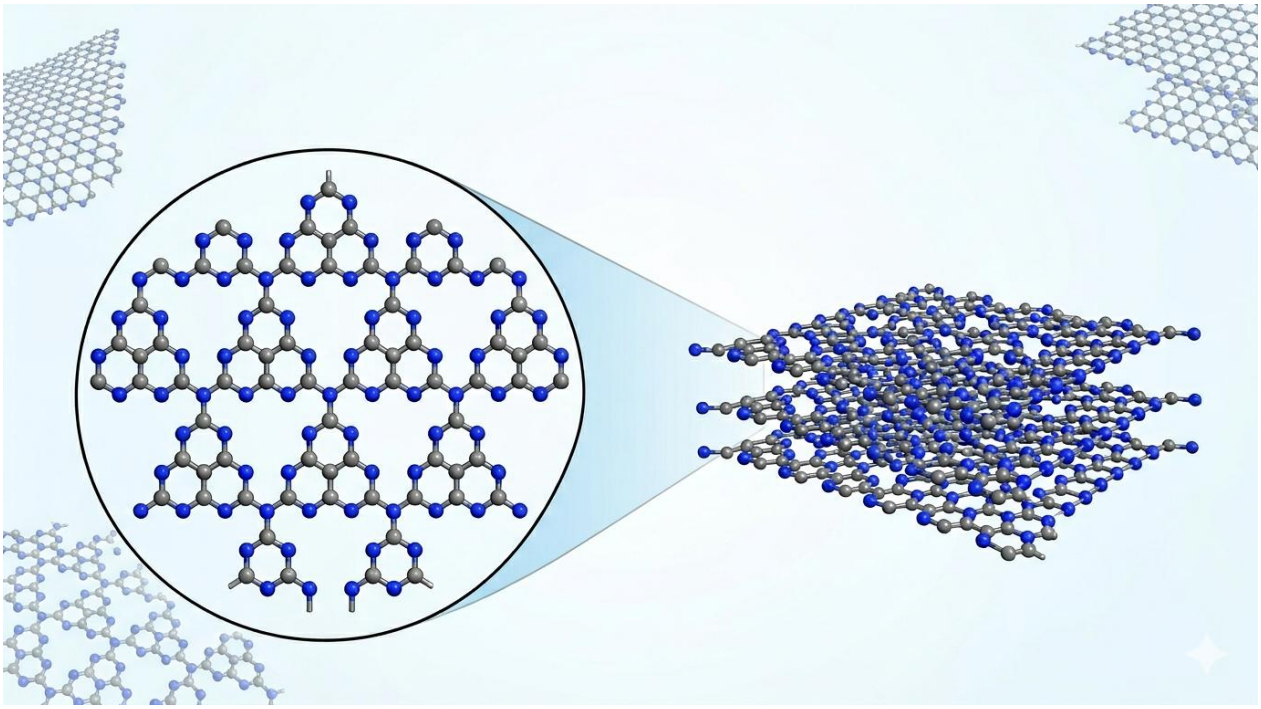

Figure 01: Physical and chemical properties of g-C_3N_4

I- 2.4. Its applications:

I-2.4.1 • Photocatalytic degradation of organic pollutants in water:

Definition: A photochemical process that uses g-C_3N_4 as a catalyst to break down toxic organic molecules (such as dyes, pesticides, and pharmaceuticals) into less harmful substances like CO_2 and H_2O.

Explanation: When g-C_3N_4 is exposed to visible light, photogenerated holes react with water to produce highly oxidizing hydroxyl radicals (•OH), which attack and decompose organic pollutants. This technology is promising for wastewater treatment [19,22,26].

I- 2.4.2 • Carbon dioxide (CO_2) reduction to chemical fuels:

Definition:

Converting carbon dioxide, a major greenhouse gas, into useful chemical compounds such as methane (CH_4), methanol (CH_3OH), or carbon monoxide (CO) using solar energy.

Explanation: The photogenerated electrons reduce adsorbed CO_2 molecules through various pathways, turning them into hydrocarbons that can be used as fuel. This application helps mitigate climate change while producing renewable energy [19][22][37].

I- 2.4.3 • Water disinfection and elimination of harmful microorganisms:

Definition: Using the oxidative properties of g-C_3N_4 to kill or inactivate bacteria, viruses, and other harmful microorganisms in water.

Explanation: The generated holes and free radicals (such as •OH and $•O_2^-$) damage the cell walls and DNA of microorganisms, leading to their death. This is an effective, chemical-free disinfection method [15,16,38].

I- 2.4.4 • Chemical and biological sensors:

Definition:Utilizing the change in electrical or optical properties of g-C_3N_4 upon interaction with specific molecules to detect their presence and measure their concentration with high accuracy. Explanation: g-C_3N_4 has a large surface area and active functional groups (-NH, -NH_2) that allow it to bind with target molecules. Upon adsorption, the material's conductivity or fluorescence intensity changes, which can be measured to identify pollutants or biomarkers [19][35].

I- 2.4.5 • Heavy metal removal from water:

Definition: Using g-C_3N_4 to reduce toxic heavy metal ions (e.g., Hg^{2+}, Cr^{6+}, Pb^{2+}) from aqueous solutions to less toxic or precipitable forms.

Explanation: The photogenerated electrons reduce Cr^{6+} to Cr^{3+}, lowering toxicity and facilitating precipitation. The amine-rich surface also adsorbs metal ions [15,26].

I- 2.4.6 • Plastic photodegradation:

Definition: Using g-C_3N_4 to convert plastic waste (e.g., polyethylene, PET) into smaller degradable fragments or useful intermediates under visible light.

Explanation: Strong photogenerated holes break long polymer chains via oxidation, reducing plastic mass and facilitating subsequent biodegradation [16][39].

I- 2.4.7 • Selective organic transformations:

Definition: Using g-C_3N_4 as a photocatalyst to convert simple organic molecules into high-value chemicals (e.g., alcohols to aldehydes, amines to imines) under mild light conditions. Explanation: The tunable redox potentials of electrons and holes activate specific bonds (C-H, O-H) without strong oxidants or high heat, enabling green synthesis of pharmaceuticals [21,31].

I- 2.4.8 • Construction materials enhancement:

Definition: Adding g-C_3N_4 to paints, cement, or coatings to impart self-cleaning, antibacterial, or air-purifying properties.

Explanation: When incorporated into building facades, sunlight triggers decomposition of airborne pollutants (NO_x, VOCs) and organic dirt, contributing to ambient air purification [22,34].

I-2.4.9 • Biomedical applications (photodynamic therapy):

Definition: Using g-C_3N_4 nanoparticles in photodynamic therapy to generate reactive oxygen species that kill cancer cells upon light exposure.

Explanation: Upon visible light irradiation, g-C_3N_4 produces ROS that selectively destroy tumor cells with minimal damage to healthy tissues [15,40].

I- 3.Titanium dioxide compound (TiO_2) :

I-3.1 . Definition:

TiO_2 is an inorganic chemical compound characterized by high chemical stability and unique optical properties, and it is one of the most widely used materials in photocatalysis [15,20,16]. It is a wide-band-gap semiconductor (anatase: ~3.2 eV, rutile: ~3.0 eV) that is active mainly under ultraviolet light ($\lambda < 387$ nm for anatase). Despite its wide band gap, TiO_2 exhibits strong surface adsorption sites for water and oxygen, leading to high photocatalytic activity. It exists in three main crystalline phases: anatase (tetragonal, most active), rutile (tetragonal, most stable), and brookite (orthorhombic, rare) [41,18, 42]. The anatase phase is considered the most active in photonic applications due to its higher conduction band edge (stronger reduction potential) and surface defects that facilitate reactions [16,43,44].

I.3.2. Historical overview:

Titanium was discovered in 1791 by the British mineralogist William Gregor. Later, it was named by the German chemist Martin Klaproth after the Titans of Greek mythology, reflecting its

strength and prominence. Titanium dioxide (TiO_2) was initially used as a white pigment in various industries due to its high refractive index and brilliant whiteness. Its photocatalytic properties were discovered later, with a landmark achievement in 1972 when Fujishima and Honda successfully demonstrated water splitting on a TiO_2 electrode under ultraviolet (UV) light. This discovery opened the door for extensive research in environmental and energy applications [24,46]. Since then, TiO_2 has been widely studied for applications including air and water purification, self-cleaning coatings, and solar cells. Recent efforts have focused on doping TiO_2---for example, with nitrogen or carbon---to extend its photocatalytic activity into the visible light region, thereby improving its efficiency under sunlight [47,42,48].

I- 3.3. Crystal structure:

Titanium dioxide (TiO_2) exists in three main crystalline phases: anatase, rutile, and brookite [41]. In all of these phases, the titanium atom is surrounded by six oxygen atoms arranged in an octahedral structure, which confers structural stability to the material [41]. Anatase has a tetragonal lattice with lattice parameters a = 3.784 Å and c = 9.515 Å. It remains stable up to approximately 700°C, above which it transforms into rutile. Rutile, characterized by tetragonal parameters a = 4.593 Å and c = 2.959 Å, is the thermodynamically stable phase at high temperatures (exceeding 700°C). Due to its high stability and brightness, rutile is widely used as a white pigment. Brookite possesses an orthorhombic structure, but it is rarely used in practical applications because of the difficulty involved in its synthesis. Among the three phases, anatase is considered the most active in photonic applications [16,18,45].

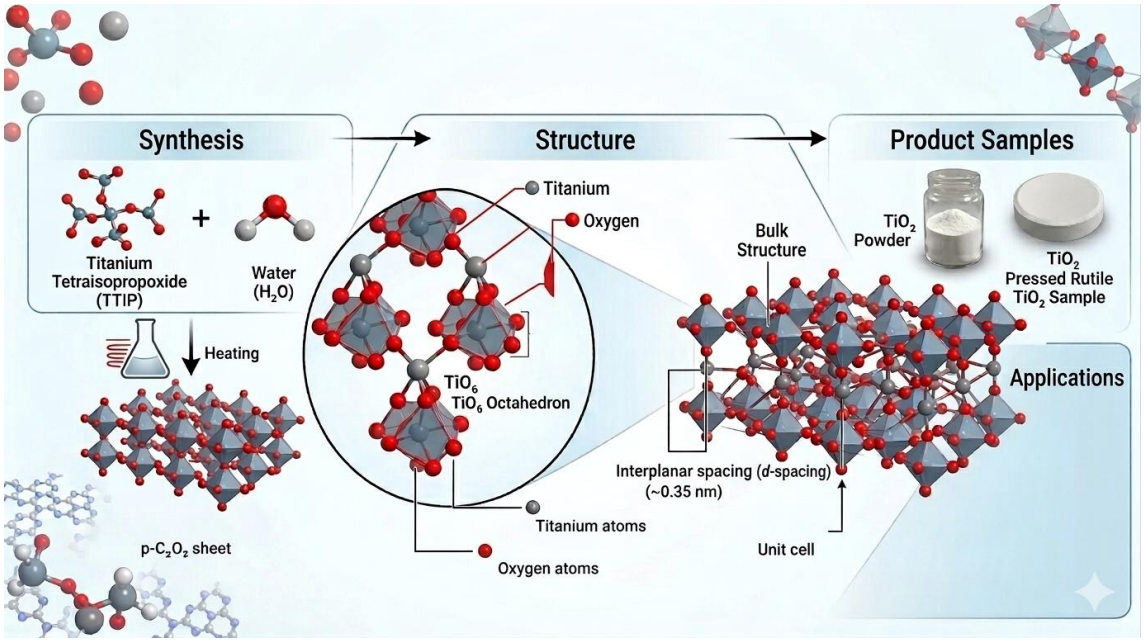

Figure 02: Physical and chemical properties of TiO_2

I- 3.4. Applications:

I-3.4. 1• Air and water purification via photocatalysis:

Definition: A heterogeneous photocatalysis process that uses TiO_2 to decompose organic and inorganic pollutants dissolved in water or present in air, converting them into harmless substances.

Explanation: When TiO_2 is exposed to UV light, strong electron-hole pairs generate hydroxyl radicals (•OH), among the strongest oxidants, which attack any organic pollutant (e.g., benzene, formaldehyde, solvents) and break it down into CO_2 and H_2O. This technology is used in air sterilizers, water purifiers, and self-cleaning coatings [15,16,38].

I- 3.4. 2• Dye-sensitized solar cells (DSSCs) :

Definition: A type of solar cell (also known as Grätzel cells) that uses a porous layer of TiO_2 nanoparticles to absorb a light-sensitive dye and transport the resulting electrons.

Explanation: The dye absorbs visible light and injects electrons into the conduction band of TiO_2. TiO_2 (thanks to its large surface area and electron-transport properties) transfers these electrons through the external circuit to generate electric current. These cells are a low-cost alternative to conventional silicon cells [36,45].

I- 3.4. 3• White pigment in chemical industries:

Definition: Using TiO_2's high light-scattering ability and brilliant whiteness to provide opaque white color to paints, plastics, paper, toothpaste, and cosmetics.

Explanation: TiO_2 (especially the rutile phase) has a very high refractive index, meaning it scatters visible light extremely efficiently. When added to a paint or plastic, it makes the material appear brilliantly white and opaque. This is the largest industrial application of TiO_2 by volume [20,42].

I-3.4. 4• Medical applications and cosmetics:

Definition: Using TiO_2's properties as a UV blocker and antibacterial agent in sunscreens, ointments, and skincare products.

Explanation: As a UV blocker, TiO_2 nanoparticles absorb UV radiation (UVA and UVB) and dissipate it as heat, preventing skin damage. As an antibacterial agent, upon light exposure, TiO_2 generates reactive oxygen species (ROS) that kill bacteria and fungi, making it useful in wound dressings and antimicrobial coatings [16,44].

I-3.4. 5• Superhydrophobic coatings:

Definition: Using TiO_2 nanoparticles to create surfaces with water contact angles >150°, causing water to bead and roll off, carrying dirt with it.

Explanation: After UV treatment, TiO_2 becomes superhydrophilic, but when chemically modified with fluoroalkylsilanes, it becomes superhydrophobic. These coatings are used in anti-fogging glass, self-cleaning surfaces, and water-repellent textiles [18,43,45].

I-3.4. 6• Perovskite solar cells:

Definition: Using TiO_2 as an electron transport layer (ETL) in perovskite solar cells, which have achieved record power conversion efficiencies.

Explanation: The mesoporous TiO_2 layer absorbs the perovskite material and efficiently transports photogenerated electrons to the electrode while preventing charge recombination [36,47,48].

I-3.4.7• Green ammonia synthesis:

Definition: Using TiO_2 as a photocatalyst to reduce atmospheric nitrogen (N_2) to ammonia (NH_3) under ambient conditions, as a clean alternative to the energy-intensive Haber-Bosch process.

Explanation: Photogenerated electrons break the strong triple bond of N_2 stepwise and provide protons (H^+) to form NH_3. TiO_2 can be combined with noble metals or carbon materials to improve efficiency [16,49,37].

I-3.4. 8• Pharmaceutical waste degradation:

Definition: Using TiO_2 to decompose pharmaceutical residues (e.g., antibiotics, anti-inflammatories, contraceptives) that resist conventional wastewater treatment.

Explanation: Hydroxyl radicals (•OH) generated on TiO_2 surfaces oxidize complex drug molecules into CO_2, H_2O, and simple harmless ions. This is effective for emerging micropollutants [17,47,39].

I-3.4. 9• Gas sensors:

Definition: Using thin TiO_2 films to detect toxic or explosive gases such as H_2, CO, and NO_x at elevated temperatures or at room temperature with UV assistance. Explanation: Adsorption of target gas molecules changes the electrical resistance of TiO_2. UV illumination accelerates this response by generating electron-hole pairs that interact with the gas. These sensors are sensitive, fast, and low-cost [18,50,44].

I-3.4. 10• Cultural heritage protection:

Definition: Applying transparent TiO_2 nanoparticle solutions to protect wall paintings and stone monuments from pollution and microorganisms.

Explanation: The thin, invisible TiO_2 layer decomposes organic pollutants and kills bacteria without altering the original appearance of the artwork [15,38].

I-4. Conclusion :

It is clear that semiconducting materials, especially g-C_3N_4 and TiO_2, play an important role in photocatalysis and the treatment of environmental pollutants, due to their distinctive properties and high efficiency. g-C_3N_4 excels in visible-light absorption and low-cost production, while TiO_2

offers superior oxidation power and chemical stability. However, each suffers from individual limitations such as rapid charge recombination (g-C_3N_4) or poor visible-light utilization (TiO_2). Therefore, their combination in composite materials (g-C_3N_4/TiO_2) improves charge separation efficiency and increases the effectiveness of photoreactions under solar light, making them among the most promising materials in environmental applications and sustainable energy [16,22,24, 49,37,51].

CHAPTER TWO: CHARACTERIZATION TECHNIQUES

II – 1. Introduction:

Analytical techniques are considered fundamental elements in scientific research, as they are used to process and interpret data with the aim of achieving accurate and reliable results. Its importance lies in its ability to transform raw data into meaningful information, which helps in understanding phenomena and discovering relationships between variables. These techniques mainly vary between quantitative and qualitative methods, in addition to mixed approaches that combine both [19]. On one hand, quantitative techniques rely on statistical processing and numerical data, and include descriptive analyzes such as calculating means and standard deviations, inferential analyzes like hypothesis testing, and correlational analyzes to measure relationships between variables [17]. On the other hand, qualitative techniques focus on interpreting meanings and contexts thru non-numeric data, and include methods such as thematic analysis to identify recurring patterns in texts, narrative analysis to study stories and life experiences, and phenomenological analysis to understand the essence of phenomena as experienced by individuals [15,24]. Qualitative analysis is considered a process aimed at constructing interpretive readings, that is, attributing meaning to social and human phenomena that are characterized by a high degree of complexity [15, 23]. The choice of the appropriate technique between quantitative, qualitative, or mixed methods depends on the nature of the study and its objectives, as well as the questions posed and the type of data to be analyzed [19,18]. Mastering these techniques and applying them accurately is a necessary step to ensure the quality of scientific research and the objectivity of its results, which contributes to the reliable development of knowledge.

II- 2.The purpose of using BET:

II-2.1.Definition:

The BET technique is widely used in characterizing solid materials, especially porous materials, powders, and catalysts. One of the main objectives of this technique is to accurately determine the specific surface area, a property that is directly related to the surface activity of the material. It also aims to study the properties of porosity, including pore size and distribution, and to analyze the adsorption behavior of different materials, which is crucial for understanding the mechanism of surface interaction with gasses or solutions. The technique is also used to evaluate the efficiency of materials used in chemical catalysis processes, as a large surface area provides more active sites. Finally, BET allows for the comparison of material properties before and after thermal or chemical

treatment, which helps in improving manufacturing processes. Thanks to these multiple objectives, BET is a fundamental technique in the fields of catalysis, water treatment, materials science, and energy storage [21,26].

II-2.2 .What the BET device reveals:

BET analysis provides a wealth of information about the surface and porosity characteristics of the solid material. Here is a detailed breakdown of the most important information:

II-2.2.1• Specific Surface Area:

specific surface area is considered one of the most important direct results of BET analysis, and it represents the total surface area of the material per unit mass, measured in m^2/g. It is calculated by determining the volume of gas required to form a complete monolayer on the external and internal surfaces of the open pores. This value is considered a crucial factor in evaluating the efficiency of catalytic materials, adsorbent materials, and thin films, as the larger the surface area, the greater the ability to react or adsorb. For example, highly porous materials such as zeolites and activated carbon exhibit surface areas that can reach thousands of square meters per gram [22].

II-2.2.2• Total Pore Volume :

The total pore volume (Pore Volume) refers to the total volume of the pores within the material per unit mass, and it is usually expressed in cm^3/g. This measurement is derived from the amount of gas adsorbed at a relative pressure close to 1 (near saturation pressure), where all the pores are filled with the liquefied gas. The pore volume is an important indicator of the material's absorptive capacity, whether in adsorption applications (such as the absorption of pollutants or gasses) or in fuel or drug storage applications. In addition, pore size helps in estimating the apparent density of the material and understanding its mechanical behavior [21].

II-2.2.3•Distribution of Pore Size:

It is not enough to know the average pore size; it is essential to understand how pore sizes are distributed within the material. BET analysis (using additional methods such as BJH -- Barrett-Joyner-Halenda) reveals the pore size distribution, allowing for the classification of pores according to the International Union of Pure and Applied Chemistry (IUPAC) into three main categories: • Micropores: Their diameters are less than 2 nanometers, and they are often found in zeolites and activated carbon, characterized by strong adsorption forces. • Mesopores: Their

diameters range between 2 and 50 nanometers, and they are common in silica gels and porous membranes, playing a role in material transport. • Large pores (Macropores): Their diameters are greater than 50 nanometers, and they function as channels for the distribution of gasses or liquids. The pore size distribution is essential for designing materials with improved performance, such as shape-selective catalysts [26].

II-2.2.4• Pore Shape:

Through the shape of the adsorption and desorption curve (especially the hysteresis phenomenon), the predominant pore shape in the material can be inferred. For example: • The cylindrical pores open at both ends provide a feedback loop of type H1. • Pores with cracks or irregular bodies give rise to other types such as H2 and H3. • Partially closed spherical pores may exhibit different behavior. The analysis of pore shape helps predict the material's behavior in practical applications, such as ease of fluid drainage or resistance to clogging [22,26].

II-2.2.5• Isotherm Type:

The adsorption curve (the relationship between the amount of adsorbed gas and the relative pressure) is classified according to the IUPAC classification into six basic types (I, II, III, IV, V, VI). The type of isotherm reveals the nature of the surface and the interaction between the material and the adsorbed gas, as well as the porosity of the material. For example: • The Type I (Langmuir) isotherm indicates a material with monolayer micropores. • Type II appears in non-porous materials or those with large pores with multilayer adsorption. • Type IV is characteristic of mesoporous materials and contains a hysteresis loop. • Type V is less common and indicates a weak interaction between the gas and the surface. Determining the type of isotherm is a crucial first step in interpreting the surface properties of the material and selecting the appropriate mathematical model for calculating the surface area [26].

II-2.2.6• The device:

Figure 03: Brunauer Emmett and Teller(BET)

II- 3.X-ray diffraction (XRD) :

II-3.1.Definition:

X-rays are a form of electromagnetic radiation whose wavelengths fall between 0.01 and 10 Å. This non-destructive approach is the most prevalent and widely adopted technique for characterizing the properties and structure of crystalline materials. Additionally, X-ray diffraction offers insight into physical attributes of the crystal, including its dimensions and orientation [55].

II-3.2. IPrinciple:

This method depends on the interaction between the crystalline structure of a specimen and short-wavelength monochromatic radiation. A monochromatic X-ray beam is aimed at a polycrystalline sample and strikes the crystal lattice planes. At these planes, the beam interacts with the electron clouds surrounding the atoms that constitute the plane. Consequently, the X-ray beam may be partially reflected by the first plane, or, if it passes without obstruction, it can continue and

undergo partial reflection from the second plane. These planes are separated by specific distances that depend on the material being examined (referred to as the interplanar spacing). The interference of the beams can be either constructive or destructive. Bragg's law allows the identification of the directions in which constructive interference occurs, which appear as diffraction peaks [55].

***Bragg's law:**

When a crystalline substance is exposed to X-radiation of wavelength λ at an incidence angle θ, diffraction takes place if Bragg's law is satisfied, as depicted in Figure 5.

$$n\lambda = 2d\_hkl\ sin\theta$$

Where: • n is an integer representing the order of reflection.

• λ is the wavelength of the X-rays.

• d is the interplanar distance.

• θ is the X-ray incidence angle.

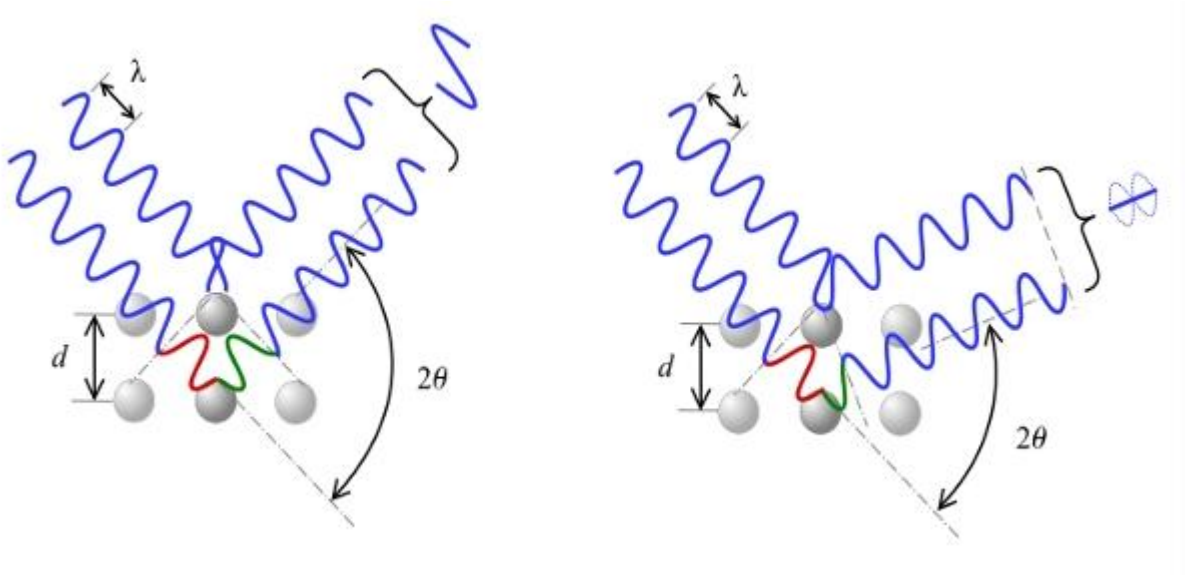

Figure 04: Diagram illustrating the principle of Bragg's law [60].

Typically, a diffractogram records the diffracted intensity as a function of the angle 2θ relative to the direct beam. Examination of the diffractogram allows the extraction of substantial

information regarding the structural and microstructural features of the sample, such as crystalline phases, crystallite size (D), crystallinity index (CrI), and crystallite morphology.

***Crystallite size determination (D):**

Although numerous approaches have been reported for size determination via XRD, the Debye-Scherrer equation remains the most frequently employed for estimating crystallite size [56].

$$D = k\lambda / (\beta \cos\theta)$$

Where: • D is the grain size expressed in nanometers. • λ is the wavelength of the X-ray beam. • θ is the diffraction angle. • β is the full width at half maximum, given in radians.

In the present study, X-ray diffraction (XRD) was performed using a Miniflex 600 instrument equipped with Cu-Kα radiation (λ = 1.5418 Å). Diffractometer reflections were recorded at ambient temperature, and the 2θ range was scanned from 10° to 80°.

***Crystallinity index (CrI):**

The crystallinity index (CrI) was derived from the XRD patterns according to the Segal method [57]:

$$CrI\ (\%) = ((I_{002} - I_{am}) / I_{002}) \times 100$$

Here, I_{002} represents the maximum diffraction intensity of the (002) lattice plane, and Iam denotes the diffraction intensity.

II-3.3• The device:

Figure05:X-ray diffraction (XRD)

II 4.- Scanning electron microscopy (SEM) :

II -4. 1.Definition:

Scanning electron microscopy (SEM) is a technique that enables the visualization of the surface morphology of solid materials. It is an analytical procedure that scans a specimen with an electron beam at high magnifications to generate high-resolution, magnified images for analysis and to precisely measure extremely small objects. This method proves highly effective for microanalysis and failure analysis of solid inorganic substances, thus offering significant advantages in morphological and dimensional characterization.

The morphology of the samples was examined using a TESCAN VEGA3 scanning electron microscope (SEM), which is equipped with a system for chemical element determination (EDS).

II -4. 2.Principle:

Scanning electron microscopy relies on electron-matter interactions to examine the surface topography of bulk samples. SEM produces images of the sample surface based on electron scattering. These images are primarily formed using surface electron emissions, namely secondary

electrons and backscattered electrons. The interaction between the primary electron beam (energy E0) and the sample generates low-energy electrons referred to as "secondary electrons." These are subsequently accelerated toward a detector that amplifies the received electrical signal (at each point, the intensity is converted into an electrical signal). Different particles are analyzed by distinct detectors, allowing the reconstruction of a three-dimensional image of the surface. In addition, this technique utilizes other primary electron--sample interactions, including the emission of backscattered electrons, absorption of primary electrons, and the generation of X-ray photons. Each of these interactions often provides valuable information about surface topography and composition, as well as insights into the relationships among different structural features of the material [58].

Strictly speaking, SEM is not a conventional microscope in the optical sense:

• No image is formed by an objective lens (as in optical microscopy or transmission electron microscopy).

• Instead, the image is built sequentially by scanning the sample surface with an electron beam and collecting secondary electrons or backscattered electrons [59].

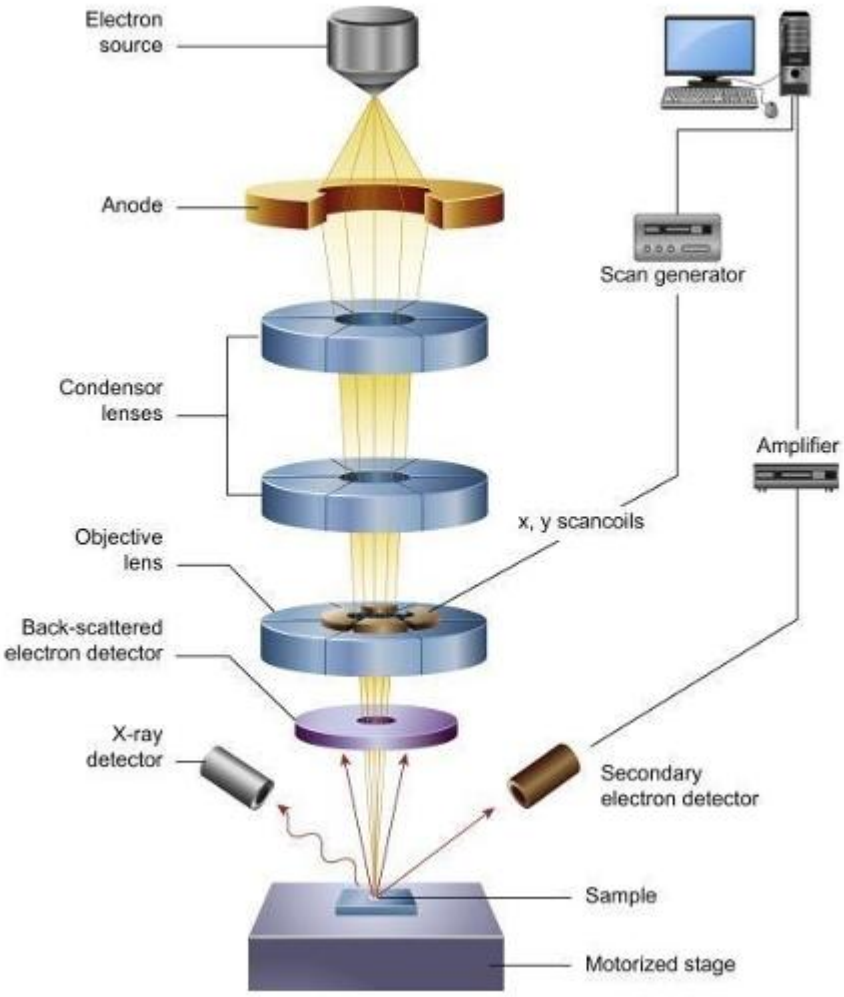

Figure 06: Schematic diagram of a scanning electron microscope [60].

II -4. 3• The device:

Figure07: Scanning Electron Microscope(SEM)

II 5- UV-visible absorption spectroscopy (UV-Vis) :

II -5.1.Definition:

Ultraviolet-visible (UV-vis) spectroscopy is employed to acquire absorbance spectra of a compound either in solution or in solid form. Spectroscopically, what is observed is the absorption of light energy or electromagnetic radiation, which promotes electrons from the ground state to the first singlet excited state of the compound or material. The UV-vis energy region of the electromagnetic spectrum spans from 1.5 to 6.2 eV, corresponding to a wavelength range of 800 to 200 nm. These properties were investigated using UV-visible transmittance spectroscopy on a Shimadzu 3101PC double-beam spectrophotometer [61].

II -5.2. Principle:

UV-visible absorption spectrometry is based on the transition of valence electrons from a ground state to an excited state following the absorption of a UV-visible photon.

The UV spectrophotometer operates according to the Beer-Lambert law. This law states that whenever a monochromatic light beam passes through a solution containing an absorbing species, the rate of decrease in radiation intensity and the thickness of the absorbing solution are proportional to the solution concentration and the incident radiation. This relationship is expressed by the following equation [62]:

$$A = \log(I_0/I) = \varepsilon\, c\, l$$

Where: • I_0: Intensity of incident light. • I: Intensity of light transmitted through the sample solution. • c: Solute concentration. • l: Path length of the sample cell. • ε: Molar absorption coefficient.

The ratio (I/I_0) is known as the transmittance (T), and the logarithm of the inverse ratio (I_0/I) is known as the absorbance (A). Therefore:

$$A = -\log(I/I_0) = -\log T = \varepsilon\, c\, l$$

Consequently:

$$A = -\log T$$

$$A = \log(1/T)$$

*Determining the optical band gap (Eg):

According to the theory of optical energy bands (Figure09), the optical band gap (Eg) can be estimated by extrapolating the absorption edge using the Tauc relation [63]:

$$(\alpha\, h\nu) = A\,(h\nu - Eg\_opt)^n \quad (III.8)$$

Where α is the absorption coefficient, A is a constant, hν is the photon energy, n is a constant that depends on the nature of the electronic transition, and Eg_opt is the optical band gap energy. The exponent n = 1/2 corresponds to a direct allowed transition, while n = 2 corresponds to an indirect allowed transition.The energy gap was obtained from the intersection of the linear portion of the absorption edge with the energy axis.

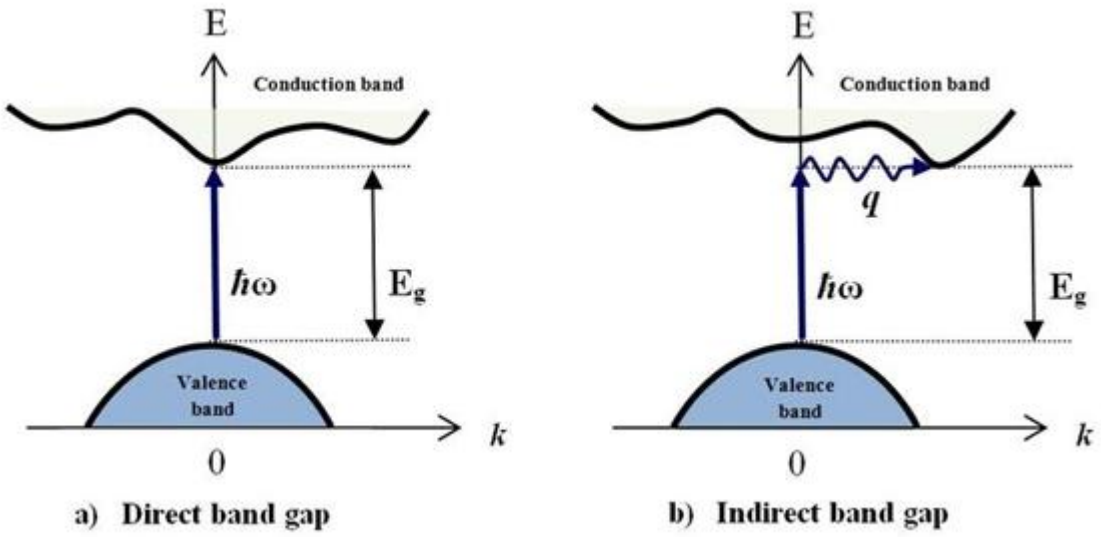

Figure 08: Electronic transitions in the case of a semiconductor with (a) an indirect band gap and (b) a direct band gap.

II -5.3• The device:

Figure09*:Ultraviolet-Visible Spectroscopy (UV-Vis)*

II – 6.Fourier transform infrared spectroscopy (FTIR) :

II -6.1.Definition:

Infrared spectroscopy permits the rapid and straightforward analysis of both organic and inorganic compounds. This technique provides information about different functional groups based on the positions of peaks in the spectrum; insights regarding nanoparticle identification and

stabilization can also be deduced from this analysis. By detecting the characteristic vibrations of chemical bonds through the absorption of infrared radiation by the material under investigation, it enables the determination of chemical functionalities present in the specimen. During analyses, the mid-infrared region between 4000 and 400 cm^{-1} is typically used [64]. The measurement is performed by depositing a layer of the product to be analyzed in contact with a crystal possessing a high refractive index, relying on the existence of an evanescent wave that propagates in a region very close to the crystal surface. Since our samples are in powder form, the required contact between the ATR crystal and the sample is achieved by applying additional pressure [64].

II -6.2. Principle:

The principle of FTIR is based on the absorption of single-beam or double-beam infrared radiation by the sample to be analyzed. Through the detection of characteristic vibrational frequencies of chemical bonds, it allows the analysis of the chemical functions present in the material.

The infrared beam is directed into a Michelson interferometer, which modulates each wavelength of the beam at a distinct frequency. Within the interferometer, the incident light beam is split into two beams by a beam splitter. These two beams are reflected off mirrors---one fixed and one movable. When the two beams recombine, destructive or constructive interference occurs depending on the position of the movable mirror. The modulated beam is then reflected from the two mirrors toward the sample, where absorptions take place. Subsequently, the beam reaches the detector, where it is converted into an electrical signal [65].

II -6.3• The device:

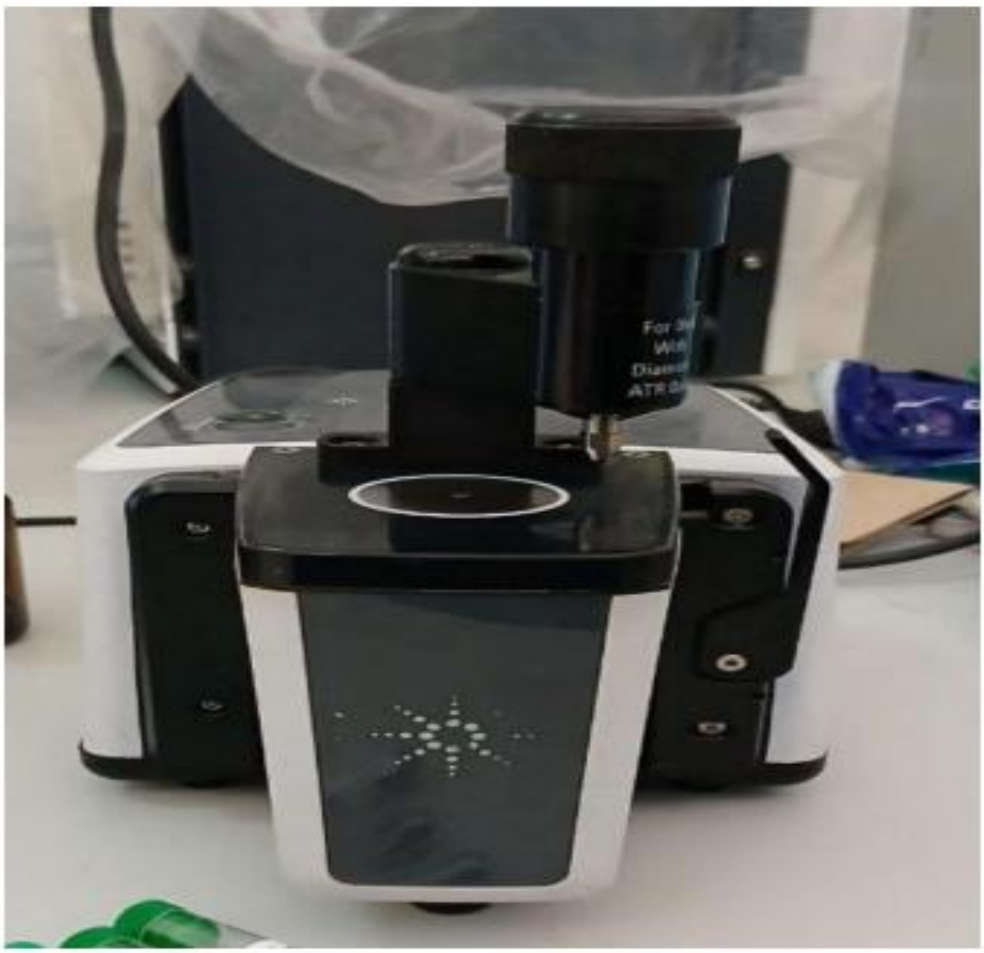

Figure10: Fourier Transform Infrared Spectroscopy (FTIR)

II- 7.Conclusion :

This chapter serves as a key reference for understanding the main analytical techniques used in material characterization, especially for nanomaterials and composites. Five techniques were presented, each with a distinct physical or chemical principle, specific objectives, and unique capabilities for revealing structural, morphological, and optical properties.

First, X-ray diffraction (XRD) was reviewed. Based on Bragg's law, it analyzes crystalline phases, determines crystallite size using the Debye-Scherrer equation, and calculates the crystallinity index via the Segal equation. XRD reveals internal structure, distinguishes phases, and estimates internal stresses and preferred orientations, making it indispensable for crystalline or semi-crystalline materials [30][31][32].

Second, scanning electron microscopy (SEM) was explained. It operates on the principle of an electron beam interacting with the sample surface, generating signals (secondary and backscattered electrons) to form high-resolution 3D images. SEM monitors surface morphology, determines particle sizes and shapes, studies phase distribution, and can be coupled with EDX for elemental analysis. It reveals fine surface details such as fiber smoothness, particle shapes (rod-like, needle-like, flower-like), and uniformity or agglomeration [27,28,29].

Third, the UV-Vis spectrophotometer was discussed. Based on the Beer-Lambert law, it measures absorption in the 200-800 nm range, exciting valence electrons. It determines absorption spectra, estimates concentrations, calculates the optical band gap of semiconductors using the Tauc relation, and studies quantum size effects in nanomaterials. UV-Vis reveals electronic and optical properties through characteristic absorption peaks and the absorption edge [33,34].

Fourth, Fourier Transform Infrared Spectroscopy (FTIR) was analyzed. It relies on the absorption of infrared light, causing bond vibrations (stretching and bending). The interference signal is transformed by Fourier transform into a spectrum identifying functional groups. FTIR identifies functional groups, compares samples, determines purity, and studies chemical reactions through peak disappearance, appearance, or shifts. It reveals characteristic bonds (OH, C=O, C-H, M-O) and bonding between components in composites [35,36].

Fifth, the BET method was reviewed. Based on physical adsorption of gases (usually nitrogen) at low temperature, it applies the BET equation to calculate specific surface area. It determines

surface area, studies porosity (pore size, distribution, shape), and analyzes adsorption behavior. BET provides precise surface area (m^2/g), classifies pores into micro, meso, and macropores, and determines isotherm type, essential for porous materials and catalysts [21,22,26].

In conclusion, these five techniques are integrated and complementary: XRD provides structural information, SEM offers morphological details, UV-Vis gives optical and electronic data, FTIR reveals chemical bonds and functional groups, and BET delivers surface area and porosity. Their combined use gives a comprehensive picture of the material from atomic to surface levels. Mastering these techniques ensures quality and reliability in materials science, chemical engineering, and nanotechnology research.

CHAPTER THREE:

HYDROGEN PRODUCTION BY PHOTO CATALYSIS

III -1. Introduction:

Hydrogen production using photocatalysis technology is considered one of the most important modern trends in the field of renewable energy. This is due to its reliance on solar energy as a primary and clean source for water splitting and the production of sustainable, emission-free fuel. This technology is gaining increasing importance in light of global challenges related to energy scarcity, environmental pollution, and the need for clean energy alternatives [37][38].

This chapter aims to provide a comprehensive and detailed study of this technology by addressing its historical development and scientific evolution, followed by a presentation of the different methods used for hydrogen production, including electrochemical, thermal, biological, and photochemical methods. It also includes an analysis of the types of catalysts used and concludes with a discussion of the main advantages and disadvantages associated with this technology.

III -2. Historical Development of Photocatalysis:

The concept of photocatalysis first appeared in 1921 by the scientist Baly, where it was associated with phenomena in which chemical reactions are accelerated under the effect of light. This concept laid the foundation for understanding the relationship between light and chemical reactions [39].

The term photocatalysis refers to two types of phenomena: the first involves chemical reactions occurring under light irradiation, while the second combines both photochemical and catalytic activities. Scientifically, photocatalysis is defined as the change in the rate of a chemical reaction or its initiation when exposed to visible or ultraviolet light in the presence of a material known as a photocatalyst [37][38].

In 1964, Doerffler and Hauffe published the first scientific study demonstrating that the presence of light with a catalyst significantly affects the reaction rate, contributing to a better understanding of this field [39].

In 1972, Fujishima and Honda achieved a major scientific breakthrough by demonstrating the possibility of water splitting on a titanium dioxide (TiO_2) electrode under ultraviolet irradiation, which opened the way for the development of photocatalytic hydrogen production [40][41].

III- 3.Hydrogen Production Methods:

III-3.1. Water Electrolysis:

Water electrolysis is one of the most widely used methods for producing green hydrogen. It relies on electricity generated from renewable sources such as solar and wind energy to split water molecules into hydrogen and oxygen [42][43].

This process is based on the molecular structure of water, composed of one oxygen atom bonded to two hydrogen atoms, which are separated using an external electric current. Electrochemical reactions occur at the electrodes. At the cathode:

$$H_2O + 2e^- \rightarrow H_2 + O^{2-}$$

At the anode:

$$O^{2-} \rightarrow \frac{1}{2}O_2 + 2e^-$$

Overall reaction:

$$H_2O \rightarrow H_2 + \frac{1}{2}O_2 .$$

There are three main types of electrolysis depending on the medium, electrolyte type, and operating temperature, as well as their environmental impact [42].

III-3.1.1•Alkaline Electrolysis:

This technique uses an alkaline solution such as potassium hydroxide (KOH) or sodium hydroxide (NaOH) as an electrolyte. Electrodes are typically made of non-noble metals such as nickel, and the system operates at moderate temperatures between 60 and 90°C. It is one of the oldest and most mature industrial hydrogen production technologies, characterized by high stability and ease of operation and maintenance. Its environmental impact is low when powered by renewable energy, with most impacts associated with equipment manufacturing [42][43].

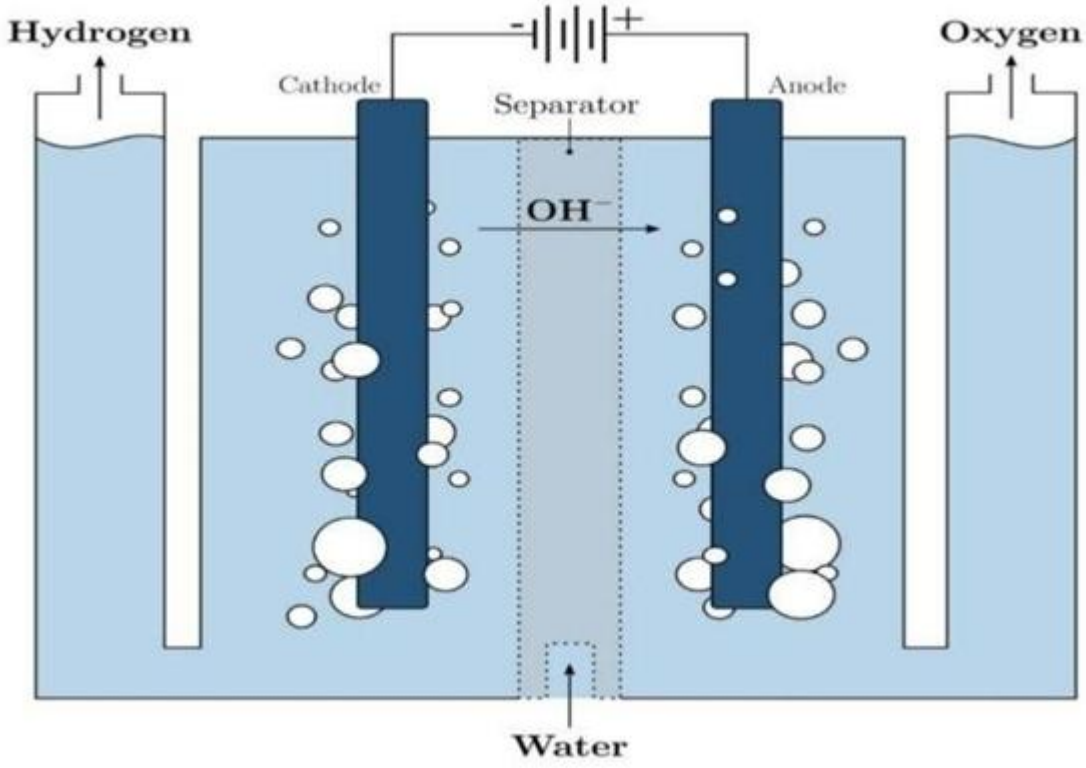

Figure 11: Alkaline Electrolyzer Cell [60].

III-3.1.2• Proton Exchange Membrane (PEM) Electrolysis:

PEM electrolysis uses a solid polymer membrane that allows only proton (H^+) transport and operates in an acidic environment. It employs noble metal electrodes such as platinum and iridium and operates at temperatures between 50 and 80°C. This technology offers high efficiency, compact design, and rapid response to electrical fluctuations, making it suitable for integration with intermittent renewable energy sources. However, its reliance on expensive noble metals increases its cost [44].

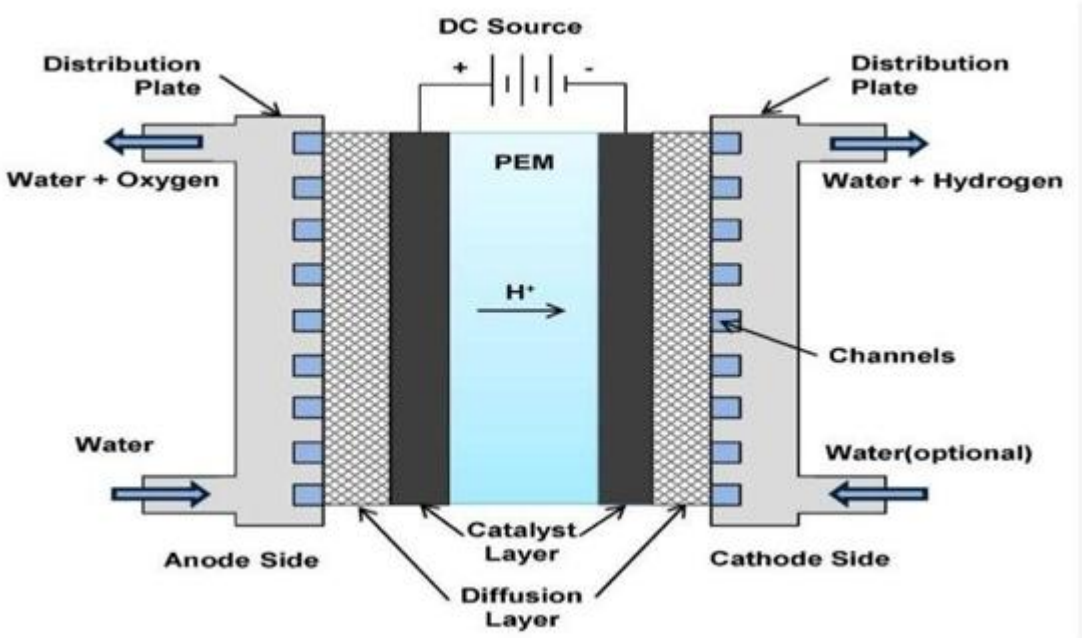

Figure 12: Proton Exchange Membrane Electrolysis[60]

III-3.1.3• Solid Oxide Electrolysis (SOEC) :

This technique uses a solid ceramic electrolyte capable of conducting oxygen ions (O^{2-}) and operates at very high temperatures up to 900°C. It allows the use of industrial waste heat, reducing electrical energy consumption and improving efficiency. Despite these advantages, high operating temperatures and advanced materials make it complex and costly [45].

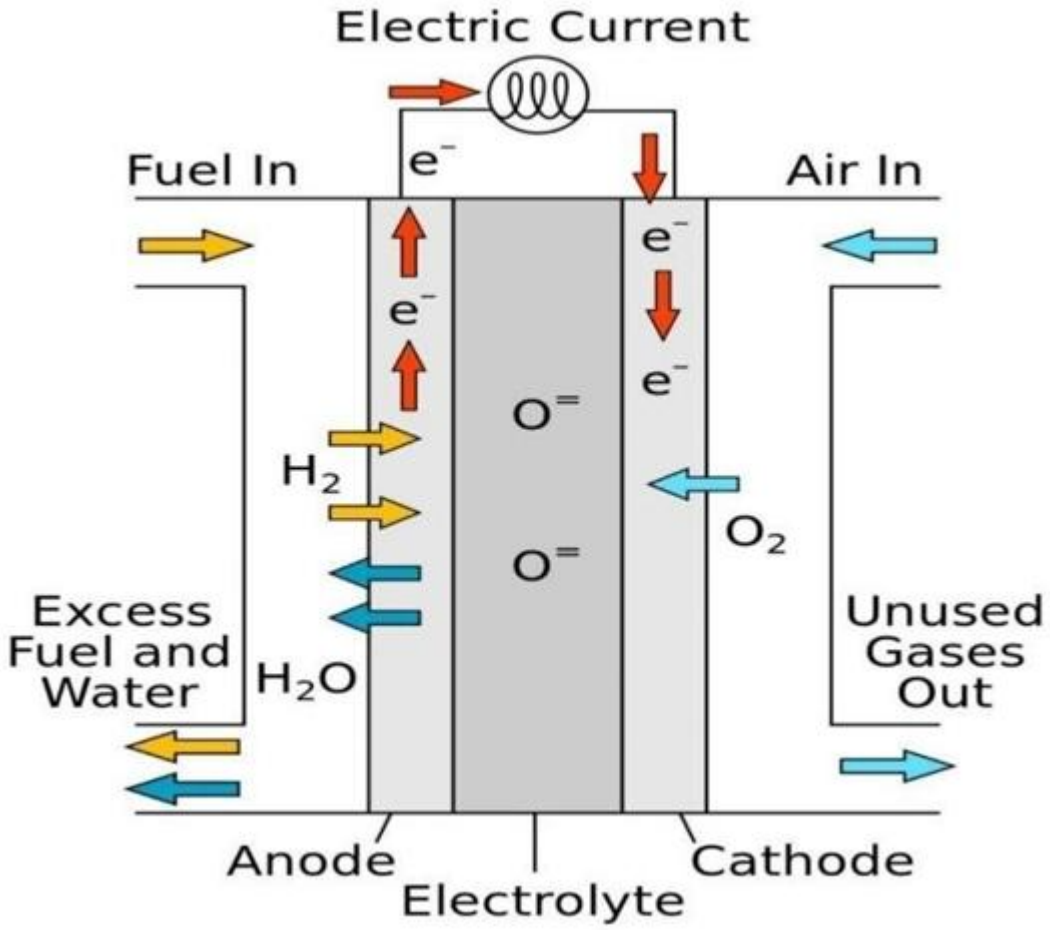

Figure 13: Solid oxide electrolysis[60].

III-3.2. Steam Methane Reforming:

Steam methane reforming is the most widely used industrial method for hydrogen production, relying on natural gas rich in methane (CH_4). The process occurs at high temperatures (700--1100°C) in the presence of a catalyst, usually nickel, producing hydrogen and carbon monoxide. Reactions:

$CH_4 + H_2O \rightarrow CO + 3H_2$ and $CO + H_2O \rightarrow CO_2 + H_2$.

Although efficient, this process produces CO_2 emissions, resulting in gray hydrogen. Environmental impact can be reduced by using biogas or carbon capture and storage (CCUS), producing blue hydrogen [43][46].

Biogas sources include agricultural waste, animal waste, organic household waste, wastewater, food industry residues, and plant waste, which are converted via anaerobic digestion into methane-rich gas [47].

III-3.3. Solar Thermochemical Water Splitting:

This method uses concentrated solar power (CSP) to generate temperatures exceeding 1000°C for thermal water splitting. Solar radiation is concentrated using mirrors or lenses onto reactors containing metal oxides such as ZnO. Reduction:

$$ZnO \rightarrow Zn + \tfrac{1}{2}O_2$$

Oxidation:

$$Zn + H_2O \rightarrow ZnO + H_2$$

This process produces no carbon emissions but faces technical challenges related to high temperatures and solar intermittency [48].

III-3.4. Photobiological Hydrogen Production:

This method uses microorganisms such as green algae and cyanobacteria to produce hydrogen using solar energy. The process involves enzymes such as hydrogenase and nitrogenase. It includes direct biophotolysis (water splitting) and indirect processes (organic compound conversion). Despite being environmentally friendly, it suffers from low efficiency and limited industrial applicability [49].

III-3.5. hotocatalysis:

Photocatalysis uses light (mainly solar) and semiconductor materials such as TiO_2, MnO_2, and Al_2O_3 to split water into hydrogen and oxygen without carbon emissions. The process starts with photon absorption, generating electron-hole pairs that drive surface reactions.

Reactions:

$$H^+ + 2e^- \rightarrow H_2 \text{ and } H_2O \rightarrow \tfrac{1}{2}O_2 + 2H^+$$

Efficiency depends on catalyst properties. Recent research focuses on carbon-based materials such as g-C_3N_4 due to their effectiveness under visible light [37][40][50][54].

III-3.6. Types of Materials:

Catalysts are classified into heterogeneous catalysts, which are solid materials where reactions occur on the surface (such as CuO, ZnS, SnO_2, ZnO, TiO_2) [40][38], and homogeneous catalysts, which are in the same phase as reactants (such as $BiVO_4$, g-C_3N_4, WO_3) [51].

III-3.7. Advantages and Disadvantages:

Green hydrogen does not produce harmful emissions during production or use, can be easily stored, and has high flexibility for conversion into electricity or synthetic fuels [42][43][52]. However, it requires large energy input and poses safety risks due to its flammability, requiring strict safety measures [42][43].

IV- 4. Conclusion:

This chapter demonstrates that photocatalytic hydrogen production represents a promising and sustainable technology for clean energy generation, primarily due to its reliance on abundant solar energy and its minimal environmental impact compared to fossil-fuel-based methods. The ability to split water molecules using semiconductor photocatalysts under light irradiation offers a pathway to produce hydrogen as a zero-emission fuel. However, despite significant progress, several challenges remain, most notably the low solar-to-hydrogen conversion efficiency and the limited long-term stability of many photocatalyst materials under operating conditions. These shortcomings currently restrict the large-scale industrial deployment of this technology. Consequently, ongoing research efforts are directed toward the development of novel photocatalysts with enhanced light absorption, improved charge separation, and greater resistance to photocorrosion. The design of heterojunctions, doping strategies, and nanostructuring have shown promise in overcoming these barriers. Therefore, catalyst development and material engineering remain key focal points for future research to make photocatalytic hydrogen production economically viable and practically applicable on a global scale [37][40][50][53].

PRACTICAL PART

CHAPTER ONE:

MATERIALS AND METHODS

I- 1.Materials:

Titanium dioxide (TiO_2), Graphitic carbon nitride (g-C_3N_4) ,d-g-C_3N_4 (hydrogen plasma-treated g-C_3N_4) ,Orange peels ,Lemon peels,Titanium isopropoxide (TTIP) ,Melamine ($C_3H_6N_6$) , Hydrogengas (H_2),Ethanol ,Triethanolamine (TEOA),Nitrogen gas (N_2) ,Distilled water,Benzoquinone (BQ) ,Isopropanol (IPA) ,Ethylenediaminetetraacetic acid disodium salt (EDTA-2Na) ,Silver nitrate ($AgNO_3$) , 2-Propanol , Deionized water,Fluorine-doped tin oxide glass (FTO glass) , Platinum wire (Pt wire) , Ag/AgCl electrode ,Sodium sulfate (Na_2SO_4, 0.5 M).

I- 2.Instruments:

X-ray diffractometer (XRD),FTIR spectrometer ,UV--vis diffuse reflectance spectrometer (UV--vis DRS) ,Scanning electron microscope (SEM) ,N_2 adsorption--desorption apparatus (BET) ,Gas chromatograph (GC, Agilent Technologies 7820A) ,Thermal conductivity detector (TCD) , Molecular sieve 5 Å column ,Solar simulator lamp,Centrifuge ,Hot air oven,Laboratory grinder,Sieve ,Magnetic stirrer, Hot plate ,Muffle furnace ,Low-temperature plasma reactor , Quartz boat ,Ultrasonic bath ,Agate mortar ,Closed quartz reactor ,Three-electrode rectangular quartz cell ,Xe lamp coupled with AM 1.5 solar simulator ,Drying oven,Alumina crucible.

I- 3Preparation:

I-3.1. Synthesis of TiO_2 by Dual Bio-Combustion Method:

TiO_2 nanoparticles were synthesized via a dual bio-combustion method using orange and lemon peel powders as natural fuels. Fresh orange and lemon peels were first washed thoroughly with distilled water to remove surface impurities. The peels were then dried in a hot air oven at 80 °C for 24 h. After complete drying, the peels were ground using a laboratory grinder and sieved to obtain fine powders.

For the synthesis, 5 g of dried orange peel powder and 5 g of dried lemon peel powder were mixed and dispersed in 100 mL of distilled water under magnetic stirring at 500 rpm. Subsequently, 10 mL of titanium isopropoxide (TTIP) was added dropwise into the solution under continuous stirring to form a homogeneous precursor mixture. The resulting solution was stirred for 30 min to ensure uniform mixing of the precursor and bio-derived fuels.

The mixture was then heated on a hot plate at 90 °C under continuous stirring until most of the solvent evaporated and a viscous gel was formed. Upon further heating, the gel underwent a self-

sustained combustion reaction, producing a voluminous and porous precursor powder due to the redox reaction between the titanium precursor and the organic components of the citrus peels.

The obtained combustion product was collected and ground using an agate mortar to obtain a uniform powder. The powder was then calcined in a muffle furnace at 450 °C for 2 h with a heating rate of 5 °C min^{-1} to remove residual organic species and improve crystallinity. After calcination, the sample was allowed to cool naturally to room temperature, and the resulting white powder was collected and denoted as TiO_2 [66].

I-3.2.Synthesis of g-C_3N_4 :

Graphitic carbon nitride (g-C_3N_4) was synthesized by the thermal polymerization of melamine. In a typical procedure, 10 g of melamine ($C_3H_6N_6$) was placed in a covered alumina crucible to limit the release of gaseous intermediates during polymerization. The crucible was then introduced into a muffle furnace and heated to 550 °C at a heating rate of 5 °C min^{-1} under air atmosphere.

The sample was maintained at 550 °C for 4 h to allow complete thermal condensation of melamine into graphitic carbon nitride. After the thermal treatment, the furnace was allowed to cool naturally to room temperature. The obtained yellow solid was collected and ground into a fine powder using an agate mortar. The resulting powder was denoted as g-C_3N_4 [67]

I-3.3. Plasma Treatment of g-C_3N_4 :

Defect-engineered g-C_3N_4 was prepared by plasma treatment of the as-synthesized g-C_3N_4 powder. Typically, 1.0 g of g-C_3N_4 was uniformly spread in a quartz boat and placed at the center of a low-temperature plasma reactor. Before plasma ignition, the reactor chamber was evacuated and purged several times with the working gas to remove residual air. The plasma treatment was then carried out under a continuous H_2 flow (40 sccm) at room temperature and a working pressure of approximately 40 Pa. The discharge power was maintained at 150 W, and the sample was treated for 30 min. After treatment, the reactor was allowed to cool naturally to room temperature under the same gas atmosphere. The resulting plasma-treated sample was collected and denoted as d-g-C_3N_4 [68,69].

I-3.4. Preparation of TiO_2/d-g-C_3N_4 Heterojunction Photocatalysts:

TiO_2/d-g-C_3N_4 heterojunction photocatalysts with different composition ratios were prepared by a simple mixing-assisted method. In a typical procedure, appropriate amounts of TiO_2 and plasma-treated g-C_3N_4 (d-g-C_3N_4) were dispersed in 100 mL of ethanol under magnetic stirring at 500 rpm for 30 min to obtain a homogeneous suspension. The mixture was then subjected to ultrasonic treatment for 30 min to improve dispersion and promote intimate interfacial contact between TiO_2 and d-g-C_3N_4.

After sonication, the suspension was heated at 80 °C under continuous stirring until complete evaporation of the solvent. The obtained solid was dried in an oven at 80 °C for 12 h, followed by grinding using an agate mortar to obtain a uniform powder. The resulting powder was subsequently calcined at 300 °C for 2 h with a heating rate of 5 °C min^{-1} to strengthen the interfacial interaction between TiO_2 and d-g-C_3N_4.

A series of composites were prepared by varying the TiO_2 content to 5, 10, 20, 40, and 80 wt% with respect to d-g-C_3N_4. The obtained samples were denoted as 5TiO_2/d-g-C_3N_4, 10TiO_2/d-g-C_3N_4, 20TiO_2/d-g-C_3N_4, 40TiO_2/d-g-C_3N_4, and 80TiO_2/d-g-C_3N_4, where the number represents the weight percentage of TiO_2 in the composite. Pure TiO_2, g-C_3N_4, and d-g-C_3N_4 were used as reference samples for comparison [70].

I-3.5. Characterization Techniques:

The crystalline structures of the prepared samples were analyzed by X-ray diffraction (XRD) using an X-ray diffractometer equipped with Cu Kα radiation (λ = 1.5406 Å). The diffraction patterns were recorded in the 2θ range of 10--80° with a scanning rate of 5° min^{-1} in order to identify the crystalline phases and evaluate the structural properties of the synthesized materials.

The surface functional groups and chemical bonding of the samples were investigated using Fourier transform infrared spectroscopy (FTIR). The spectra were recorded in the wavenumber range of 400--4000 cm^{-1} using the KBr pellet method.

The optical absorption properties of the prepared photocatalysts were examined using UV--vis diffuse reflectance spectroscopy (UV--vis DRS) in the wavelength range of 200--800 nm. The band gap energies of the samples were estimated using the Kubelka--Munk function derived from the diffuse reflectance data.

The morphology and surface microstructure of the prepared materials were observed using scanning electron microscopy (SEM). The SEM analysis was carried out to evaluate the particle size, morphology, and dispersion of TiO_2 on the surface of g-C_3N_4.

The specific surface area and porosity of the samples were determined by N_2 adsorption--desorption measurements using the Brunauer--Emmett--Teller (BET) method. The measurements were performed at 77 K, and the samples were degassed under vacuum prior to analysis.

I-3.6. Photocatalytic Hydrogen Evolution:

The photocatalytic hydrogen evolution experiments were carried out in a closed quartz reactor under simulated solar irradiation. Prior to irradiation, the reaction suspension was purged with nitrogen gas for 30 min to remove dissolved oxygen from the system.

In a typical experiment, 5 mg of the photocatalyst was dispersed in 20 mL of an aqueous solution containing 5 vol% triethanolamine (TEOA), which served as a sacrificial electron donor. The suspension was magnetically stirred to ensure homogeneous dispersion of the photocatalyst during the reaction.

The photocatalytic reactions were conducted under irradiation using a solar simulator lamp as the light source. Continuous magnetic stirring was maintained during the reaction to keep the photocatalyst particles uniformly suspended in the solution.

The amount of evolved hydrogen was quantified by gas chromatography (GC, Agilent Technologies 7820A) equipped with a thermal conductivity detector (TCD) set at 250 °C. Nitrogen was used as the carrier gas with a flow rate of 22.5 mL min^{-1}. Hydrogen separation was achieved using a molecular sieve 5 Å column, while the oven temperature was maintained at 50 °C [71].

I-3.7. Radical Scavenger Test:

Radical scavenger experiments were carried out under the optimized photocatalytic hydrogen evolution conditions in order to identify the main reactive species involved in the photocatalytic process and to gain insight into the charge transfer mechanism of the TiO_2/g-C_3N_4 heterojunction system. Prior to irradiation, the reaction suspension was purged with high-purity nitrogen gas for 30 min to remove dissolved oxygen and establish an anaerobic environment. In a typical experiment, 5 mg of the photocatalyst was dispersed in 20 mL of a degassed aqueous solution containing 5 vol% triethanolamine (TEOA) as a sacrificial electron donor. The suspension was

ultrasonicated for 5 min and then magnetically stirred to ensure homogeneous dispersion of the photocatalyst. To selectively quench different reactive species, appropriate scavengers were individually introduced into the reaction mixture while maintaining all other experimental parameters constant. Benzoquinone (BQ, 1 mM) was used as a scavenger for superoxide radicals ($\bullet O_2^-$), isopropanol (IPA, 10 mM) was employed to trap hydroxyl radicals (•OH), ethylenediaminetetraacetic acid disodium salt (EDTA-2Na, 5 mM) was used as a hole (h^+) scavenger, while silver nitrate ($AgNO_3$, 1 mM) was added as an electron (e^-) scavenger. Photocatalytic hydrogen evolution experiments were performed under UV irradiation using a 300 W xenon lamp, while the reaction mixture was continuously stirred at 900 rpm to maintain a uniform suspension. The amount of hydrogen produced during the reaction was quantified using gas chromatography equipped with a thermal conductivity detector (GC-TCD), following the same analytical procedure described for the hydrogen generation experiments conducted without scavengers. The hydrogen evolution rate obtained in the presence of each scavenger was then compared with that obtained in the absence of scavengers in order to determine the contribution of the corresponding reactive species to the photocatalytic hydrogen evolution mechanism [71].

I-3.8. Recycling Performance:

The stability and reusability of the photocatalyst were evaluated through recycling experiments performed under the same photocatalytic hydrogen evolution conditions described above. After each reaction cycle, the photocatalyst was separated from the reaction suspension by centrifugation at 8000 rpm for 10 min, followed by several washing steps with deionized water and ethanol to remove residual reactants and possible adsorbed intermediates. The recovered photocatalyst was then dried at 60 °C for 12 h and reused in the subsequent cycle without further treatment. This procedure was repeated for five consecutive cycles in order to assess the durability of the photocatalyst. The hydrogen evolution activity obtained in each cycle was compared with that of the initial run [71].

I-3.9. Photoelectrochemical Studies:

Photoelectrochemical measurements were carried out in a three-electrode rectangular quartz cell using the prepared samples as photoelectrodes. A fluorine-doped tin oxide (FTO) glass (1 cm^2) coated with the photocatalyst served as the working electrode, while a Pt wire and Ag/AgCl electrode were used as the counter and reference electrodes, respectively. The electrolyte consisted of an aqueous Na_2SO_4 solution (0.5 M) without pH adjustment.

The working electrode was prepared as follows. 10 mg of the photocatalyst was dispersed in 5 mL of 2-propanol and ultrasonicated for 30 min to obtain a homogeneous suspension. The resulting suspension was then drop-casted onto a 1 cm^2 FTO glass substrate and allowed to dry at room temperature overnight to obtain the photocatalyst-coated electrode.

The photoelectrochemical measurements were performed under illumination using a Xe lamp coupled with an AM 1.5 solar simulator, which served as the light source to simulate solar irradiation [72].

CHAPTER TWO:

RESULTS AND DISCUSSION

II – 1.Optical Properties:

The optical properties of the prepared samples were investigated by UV--vis spectroscopy, and the corresponding spectra are presented in Figure 1a. Pristine TiO_2 exhibits a characteristic absorption edge in the ultraviolet region at approximately 388 nm, corresponding to a band gap of 3.20 eV as derived from the Tauc plot in Figure 1b. This value is consistent with the intrinsic band gap of anatase TiO_2 reported in the literature [73]. In contrast, g-C_3N_4 displays a broader absorption extending into the visible region with a band gap of 2.70 eV, arising from the π--π* transitions within the conjugated heptazine framework [74].

After plasma treatment, d-g-C_3N_4 shows enhanced visible-light absorption accompanied by a noticeable red shift of the absorption edge (Figure 1a), with the band gap decreasing to 2.62 eV (Figure 1b). This reduction indicates that plasma treatment introduces defect-related electronic states, such as nitrogen vacancies or unsaturated surface bonds, which effectively modify the electronic structure and extend the light-harvesting capability of carbon nitride [75].

The formation of TiO_2/d-g-C_3N_4 heterostructures further alters the optical response of the system. As shown in Figure 1a, all composite samples retain the visible-light absorption of d-g-C_3N_4 while exhibiting enhanced absorption in the UV region due to TiO_2 incorporation. The band gap values gradually decrease with increasing TiO_2 content, reaching 2.55, 2.48, 2.45, 2.41, and 2.38 eV for 5TiO_2/d-g-C_3N_4, 10TiO_2/d-g-C_3N_4, 20TiO_2/d-g-C_3N_4, 40TiO_2/d-g-C_3N_4, and 80TiO_2/d-g-C_3N_4, respectively (Figure 14b).

The progressive narrowing of the apparent band gap attributed to the combined effects of plasma-induced defect states and interfacial electronic coupling within the TiO_2/d-g-C_3N_4 heterojunction, which facilitate lower-energy optical transitions and broaden the visible-light response [76]. Notably, the 40TiO_2/d-g-C_3N_4 sample presents an optimal optical profile, maintaining strong visible-light absorption while benefiting from enhanced interfacial interaction with TiO_2.

(a) (b)

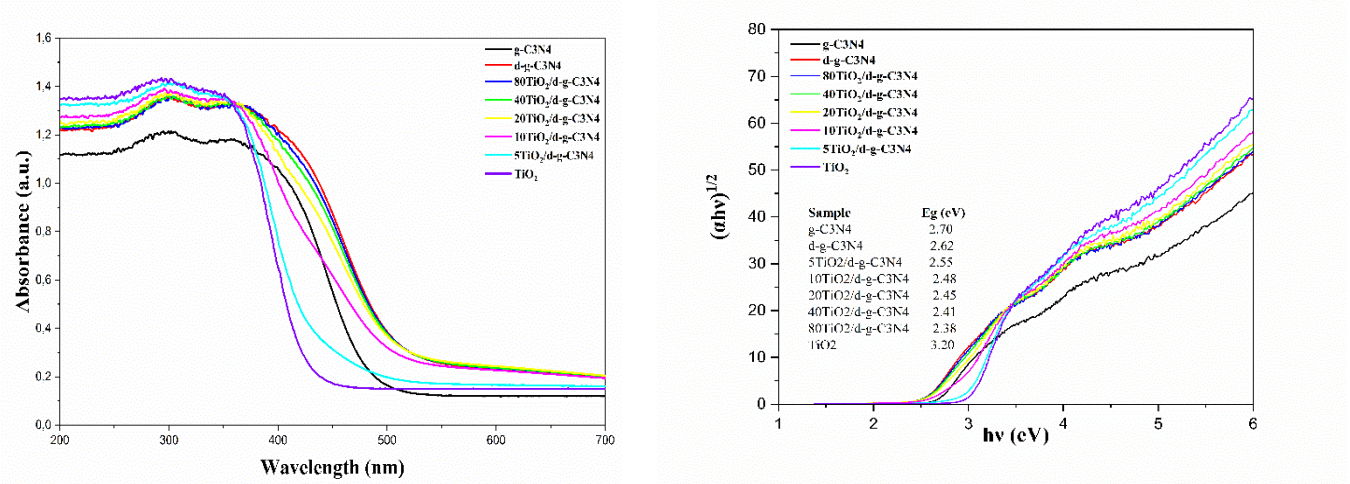

Figure 14: Optical characterization of TiO_2 by UV--vis spectroscopy: (a) UV--vis absorption spectrum; (b) Tauc plot for band gap determination.

II-2. FTIR Analysis:

The chemical structure and bonding environment of the prepared samples were investigated using FTIR spectroscopy, and the corresponding spectra are presented in Figure 15.

For g-C_3N_4, several characteristic absorption bands are observed in the region of 1200--1650 cm^{-1}, which are attributed to the typical C--N and C=N stretching vibrations of the aromatic heterocycles in the graphitic carbon nitride framework. In addition, a distinct peak located at approximately 810 cm^{-1} corresponds to the breathing mode of the triazine/heptazine units, confirming the successful formation of the polymeric g-C_3N_4 structure [77,78].

After plasma treatment, the d-g-C_3N_4 sample retains the main structural features of pristine g-C_3N_4, indicating that the overall polymeric framework remains intact. However, slight changes in the intensity of the bands within the 1200--1650 cm^{-1} region can be observed, suggesting the introduction of structural defects or surface functional groups during the plasma treatment process. Such modifications are often associated with the formation of nitrogen vacancies or unsaturated nitrogen sites, which can influence the electronic structure of carbon nitride [79].

For the TiO_2/d-g-C_3N_4 composites, the FTIR spectra display the characteristic bands of g-C_3N_4 together with a broad absorption band in the 500--700 cm^{-1} region, which is assigned to the Ti--O--Ti stretching vibration of the TiO_2 lattice [80]. The coexistence of these characteristic bands

confirms the successful coupling of TiO_2 with the d-g-C_3N_4 framework without destroying the fundamental structure of carbon nitride.

The FTIR results demonstrate that the plasma treatment introduces defect sites within the g-C_3N_4 structure while preserving its polymeric network, and that the subsequent formation of TiO_2/d-g-C_3N_4 heterostructures occurs without significant structural degradation of either component.

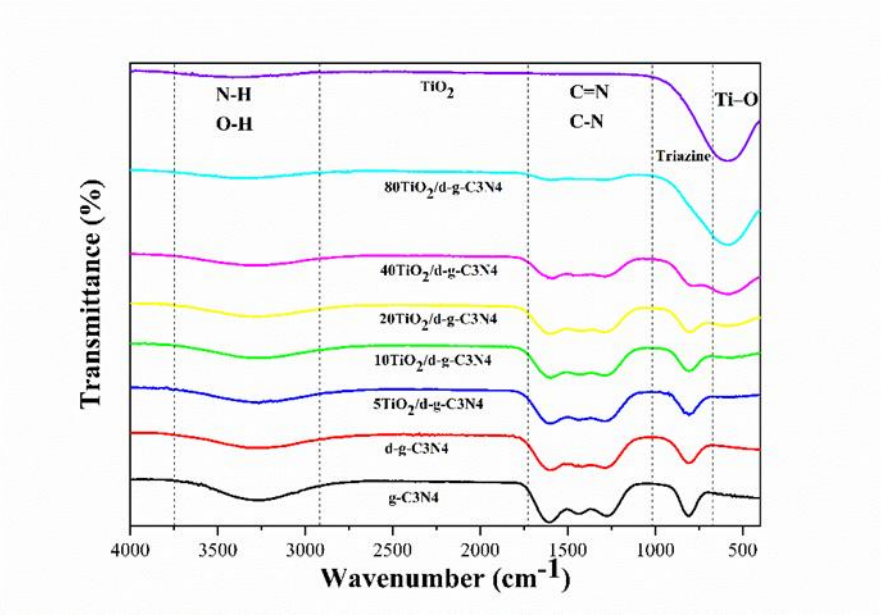

Figure 15: FTIR analysis showing the functional groups and chemical bonding of the prepared TiO_2 and g-C_3N_4 based.

II- 3.XRD Analysis:

The phase composition and crystallographic features of the prepared samples were examined by X-ray diffraction (XRD), and the corresponding patterns are shown in Figure 3. Pristine g-C_3N_4 exhibits the two characteristic reflections of polymeric carbon nitride, namely a weak peak at around 13.1° indexed to the (100) plane and a strong peak at approximately 27.2° assigned to the (002) plane [81]. The former is associated with the in-plane structural ordering of tri-s-triazine units, whereas the latter arises from the interlayer stacking of the conjugated aromatic layers in graphitic carbon nitride [82]. These features are fully consistent with the reported XRD fingerprint of g-C_3N_4 [81].

After plasma treatment, the diffraction profile of d-g-C_3N_4 remains generally similar to that of pristine g-C_3N_4, indicating that the fundamental polymeric framework is retained. However, the (002) reflection becomes broader and shifts slightly from 27.20° to 27.40°, suggesting a partial perturbation of the layered stacking order [83]. This trend is further supported by the decrease in the calculated interlayer spacing from 3.276 Å for g-C_3N_4 to 3.252 Å for d-g-C_3N_4, together with the marked reduction in crystallite size from 6.89 to 3.48 nm. Simultaneously, the lattice microstrain increases from 0.021 to 0.042, while the dislocation density rises from 0.0210 to 0.0828 nm^{-2}. Collectively, these changes indicate that plasma treatment introduces a substantial amount of structural disorder and defect sites into the carbon nitride framework without completely destroying its graphitic backbone [84]. Such behavior agrees well with literature reports showing that plasma activation of g-C_3N_4 generates defect-rich and partially disordered structures while preserving the basic XRD signature of carbon nitride [85].

The diffraction behavior of the composites evolves systematically with increasing TiO_2 loading. For 5TiO_2/d-g-C_3N_4, 10TiO_2/d-g-C_3N_4, and 20TiO_2/d-g-C_3N_4, the dominant reflection remains centered in the 27.5--27.7° region, indicating that the diffraction response is still governed mainly by the stacked carbon nitride domains [86]. In these samples, the calculated crystallite sizes remain low, in the range of 3.44--3.62 nm, while the microstrain stays relatively high (0.040--0.042). The dislocation densities are also high, between 0.0761 and 0.0846 nm^{-2}, confirming that the low-TiO_2 composites still inherit the defect-rich nature of plasma-treated g-C_3N_4. Their estimated degree of crystallinity increases only moderately from 50 to 55%, indicating that the introduction of small amounts of TiO_2 does not yet dominate the overall structural organization of the composite.

A clear structural transition occurs for 40TiO_2/d-g-C_3N_4, 80TiO_2/d-g-C_3N_4, and pure TiO_2, where the dominant diffraction peak shifts to around 25.3°, corresponding to the anatase (101) reflection. Additional anatase peaks are observed near 37.8°, 48.0°, 53.9°, 55.1°, and 62.7°, assignable to the (004), (200), (105), (211), and (204) planes, respectively, in agreement with standard anatase TiO_2 diffraction data. The increasing intensity and sharpening of these peaks with increasing TiO_2 fraction indicate progressive enhancement of the crystalline anatase contribution to the heterostructure.

This transition is quantitatively reflected in Table 1. The Scherrer crystallite size increases sharply from 3.62 nm for 20TiO_2/d-g-C_3N_4 to 7.93 nm for 40TiO_2/d-g-C_3N_4, and then further to 9.06 nm for 80TiO_2/d-g-C_3N_4, approaching 9.49 nm for pure TiO_2. The same trend is reproduced

by the Williamson--Hall crystallite size, which increases from 3.34 nm to 7.42, 8.41, and 8.83 nm, respectively. At the same time, the lattice microstrain decreases progressively from 0.040--0.042 in the low-TiO_2 composites to 0.020 for 40TiO_2/d-g-C_3N_4, 0.017 for 80TiO_2/d-g-C_3N_4, and 0.017 for pure TiO_2. Likewise, both forms of dislocation density decrease substantially as the TiO_2 content increases. This inverse relationship between crystallite size and defect density is fully expected: larger and better-ordered anatase domains produce narrower diffraction peaks, lower strain, and lower defect density. The same structural evolution is mirrored in the degree of crystallinity, which rises from 48% for d-g-C_3N_4 to 71% for 40TiO_2/d-g-C_3N_4, 78% for 80TiO_2/d-g-C_3N_4, and 82% for pure TiO_2.

For completeness, the structural parameters were estimated using the following equations.

Scherrer equation [87]:

$$D = (K\lambda) / (\beta \cos\theta)$$

Bragg law [88]:

$$n\lambda = 2d \sin\theta,\ d = \lambda / (2 \sin\theta)$$

Williamson--Hall equation [89]:

$$\beta \cos\theta = (K\lambda / D\_WH) + 4\varepsilon \sin\theta$$

Dislocation density [90]:

$$\delta\_Scherrer = 1 / (D\_Scherrer^2),\ \delta\_WH = 1 / (D\_WH^2)$$

Tetragonal lattice relation [91]:

$$1/d^2 = (h^2 + k^2)/a^2 + l^2/c^2$$

Degree of crystallinity [92]:

$$Xc(\%) = (Ac / (Ac + Aa)) \times 100$$

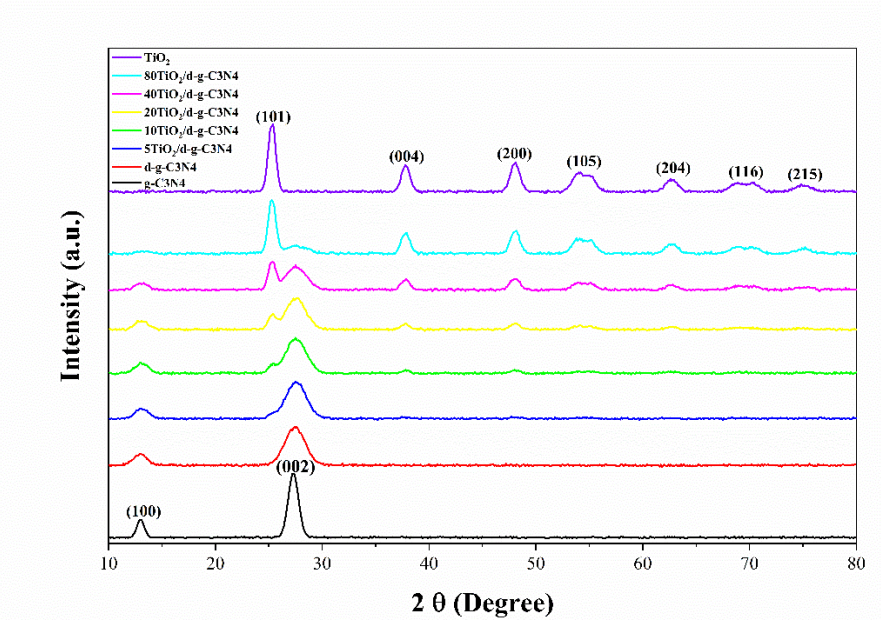

Figure 16: XRD patterns of g-C_3N_4, d-g-C_3N_4, pure TiO_2, and TiO_2/d-g-C_3N_4 nanocomposites with different weight ratio.

Table 1: Structural parameters derived from XRD analysis

Sample	Crystallite size (Scherrer) (nm)	Crystallite size (WH) (nm)	d002 spacing (Å)	Lattice parameter a (Å)	Microstrain	Dislocation density (Scherrer) (nm^{-2})	Dislocation density (WH) (nm^{-2})	Crystallinity (%)
g-C3N4	6.89	6.32	3.276	—	0.021	0.0210	0.0250	61
d-g-C3N4	3.48	3.21	3.252	—	0.042	0.0828	0.0968	48
5TiO2/d-g-C3N4	3.44	3.18	3.241	—	0.042	0.0846	0.0989	50
10TiO2/d-g-C3N4	3.54	3.27	3.241	—	0.041	0.0799	0.0935	53

20TiO2/d-g-C3N4	3.62	3.34	3.218	—	0.040	0.0761	0.0896	55
40TiO2/d-g-C3N4	7.93	7.42	—	5.36	0.020	0.0159	0.0182	71
80TiO2/d-g-C3N4	9.06	8.41	—	5.36	0.017	0.0122	0.0141	78
TiO2	9.49	8.83	—	5.33	0.017	0.0111	0.0128	82

II – 4.SEM Analysis :

The surface morphology of the prepared materials was investigated by scanning electron microscopy (SEM), and the corresponding images are presented in Figure 16. The pristine g-C_3N_4 sample (Figure 16a) exhibits a typical layered nanosheet morphology, consisting of thin, wrinkled sheets stacked into irregular aggregates. This morphology is characteristic of polymeric carbon nitride obtained via thermal polymerization of nitrogen-rich precursors, where the layered structure originates from the stacking of conjugated heptazine units [93].

After plasma treatment, the d-g-C_3N_4 sample (Figure 16b) maintains the overall layered morphology of pristine g-C_3N_4, indicating that the fundamental polymeric framework remains structurally intact. However, the nanosheets become noticeably more fragmented and rougher, and the stacking appears less compact. In addition, the presence of irregular edges and increased porosity can be observed. These changes suggest that the plasma treatment induces partial exfoliation and structural etching of the carbon nitride layers, which is consistent with the generation of defect sites observed in the structural analysis [94].

The SEM image of 5TiO_2/d-g-C_3N_4 (Figure 16c) shows that the nanosheet morphology of defect-engineered carbon nitride is largely preserved after the introduction of TiO_2. Small TiO_2 nanoparticles can be observed decorating the surface of the nanosheets, although their density

remains relatively low. The nanoparticles appear to be well dispersed across the carbon nitride framework, indicating that the TiO_2 phase is successfully anchored onto the d-g-C_3N_4 surface. The intimate interfacial contact between the two components suggests the initial formation of a heterostructured interface.

With increasing TiO_2 loading, a higher density of nanoparticles becomes evident. In 10TiO_2/d-g-C_3N_4 (Figure 14d), TiO_2 nanoparticles are more uniformly distributed across the nanosheet surface, while the layered morphology of carbon nitride remains clearly distinguishable. This indicates that the carbon nitride sheets still serve as the primary structural scaffold at this composition, while TiO_2 acts as the dispersed secondary phase.

A further increase in TiO_2 content leads to a more pronounced coverage of the nanosheets. In the 20TiO_2/d-g-C_3N_4 sample (Figure 16e), the TiO_2 nanoparticles appear more abundant and partially cover the carbon nitride sheets. Nevertheless, the underlying layered morphology is still observable, confirming that the composite retains a hybrid architecture composed of nanosheets decorated with semiconductor nanoparticles.

A significant morphological transition occurs for 40TiO_2/d-g-C_3N_4 (Figure 16f). At this composition, a large number of TiO_2 nanoparticles are distributed over the surface of the carbon nitride sheets, resulting in partial coverage of the layered structure. The increased density of nanoparticles suggests a stronger interfacial interaction between TiO_2 and d-g-C_3N_4.

When the TiO_2 loading is further increased, the morphology becomes increasingly dominated by the TiO_2 phase. In 80TiO_2/d-g-C_3N_4 (Figure 16g), densely packed nanoparticles are observed, and the layered carbon nitride structure becomes only weakly visible. The surface appears largely composed of aggregated TiO_2 nanocrystals, indicating that TiO_2 becomes the dominant structural component in the composite.

For comparison, the SEM image of pure TiO_2 (Figure 16h) reveals a morphology consisting of aggregated nanoparticles forming irregular clusters. The particles exhibit a granular appearance without any layered features, which is consistent with the morphology commonly reported for TiO_2 nanoparticles synthesized through combustion-based methods. The aggregation of nanoparticles is likely driven by the high surface energy of the nanocrystalline TiO_2 domains.

(a)

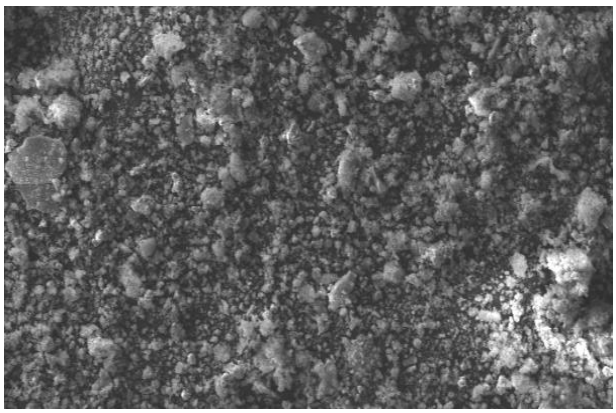

(b)

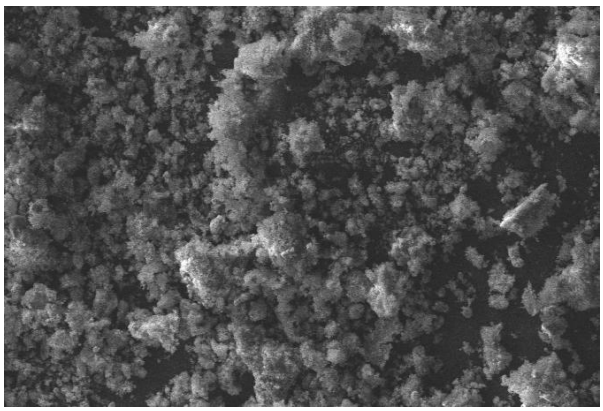

(c)

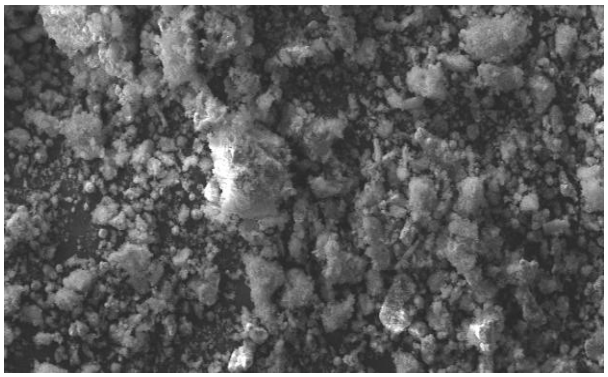

(d)

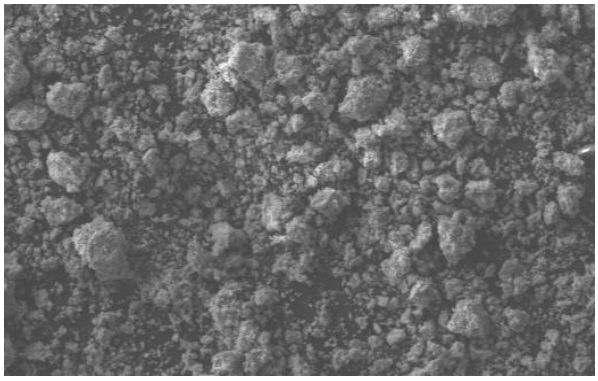

(e)

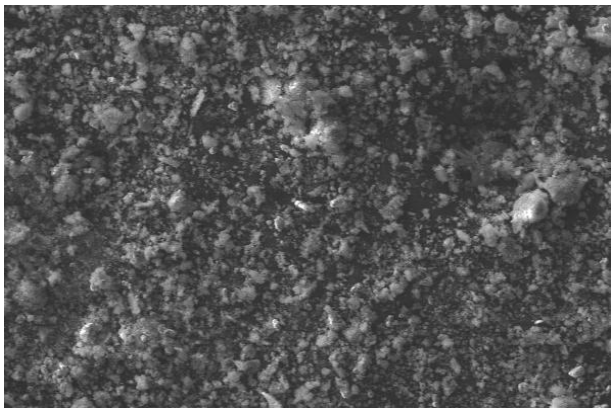

(f)

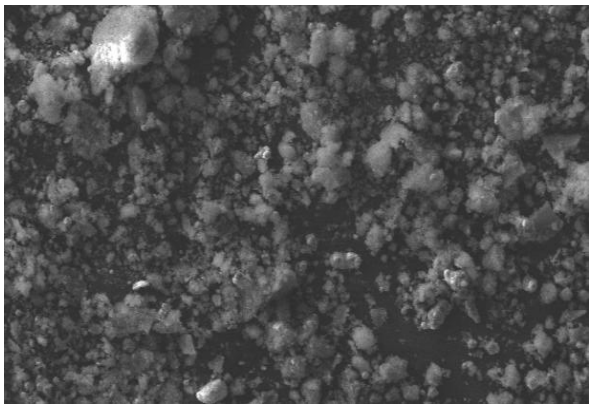

(g) (h)

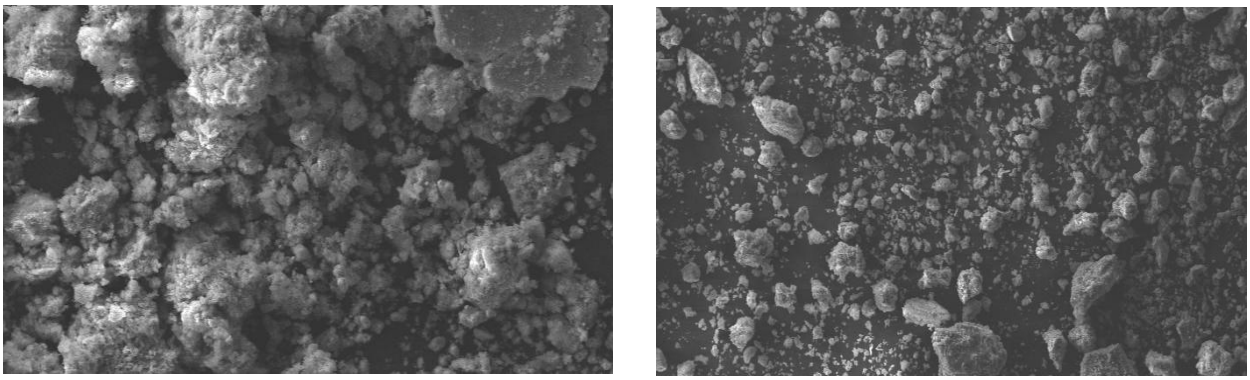

Figure 17: SEM images of (a) g-C_3N_4, (b) d-g-C_3N_4, (c) 5TiO_2/d-g-C_3N_4, (d) 10TiO_2/d-g-C_3N_4, (e) 20TiO_2/d-g-C_3N_4, (f) 40TiO_2/d-g-C_3N_4, (g) 80TiO_2/d-g-C_3N_4, and (h) TiO_2.

II – 5.BET Analysis:

The textural properties of the prepared samples were investigated by nitrogen adsorption--desorption measurements, and the corresponding parameters are summarized in Table 2. All samples exhibit type IV adsorption--desorption isotherms according to the IUPAC classification, indicating the presence of well-developed mesoporous structures [95]. Such mesoporosity provides accessible surface active sites and facilitates efficient mass transfer during photocatalytic reactions [96].

The pristine g-C_3N_4 sample exhibits a relatively low specific surface area of 16.8 $m^2 g^{-1}$, which is consistent with the compact layered structure produced during the thermal polymerization of nitrogen-rich precursors. The corresponding pore volume is 0.072 $cm^3 g^{-1}$, while the average pore diameter lies in the mesoporous range (17--18 nm). This relatively limited surface area originates from the strong interlayer stacking of carbon nitride sheets, which restricts the accessible surface sites [97].

Following plasma treatment, the d-g-C_3N_4 sample shows a significant increase in the specific surface area to 27.4 $m^2 g^{-1}$, accompanied by a higher pore volume (0.103 $cm^3 g^{-1}$) and a reduced particle size. This evolution reflects the structural etching and partial exfoliation of the carbon nitride layers induced by plasma activation, which generates additional surface defects and porosity while improving the accessibility of the nanosheet surfaces.

The incorporation of TiO_2 nanoparticles further modifies the textural properties of the system. In the $20TiO_2$/d-g-C_3N_4 composite, the specific surface area increases to 38.6 $m^2\ g^{-1}$, together with an increased pore volume of 0.136 $cm^3\ g^{-1}$. This enhancement arises from the dispersion of TiO_2 nanoparticles on the carbon nitride nanosheets, which effectively suppresses the restacking of the layers and stabilizes the porous architecture.

A maximum surface area is obtained for the $40TiO_2$/d-g-C_3N_4 composite (52.1 $m^2\ g^{-1}$) along with the highest pore volume (0.184 $cm^3\ g^{-1}$). The highly dispersed TiO_2 nanoparticles create additional interparticle voids and stabilize the open nanosheet structure of defect-engineered carbon nitride. This composition therefore generates a heterostructured architecture with a large accessible interface and well-developed mesoporosity.

When the TiO_2 loading is further increased to $80TiO_2$/d-g-C_3N_4, the specific surface area slightly decreases to 44.3 $m^2\ g^{-1}$, accompanied by a reduction in pore volume. The higher concentration of TiO_2 nanoparticles promotes partial aggregation, which reduces the accessible surface area by covering part of the carbon nitride surface and partially blocking the mesopores.

For comparison, the pure TiO_2 sample exhibits the highest specific surface area (63.5 $m^2\ g^{-1}$) and the largest pore volume (0.211 $cm^3\ g^{-1}$). This high surface area is directly related to the dual combustion synthesis method employed for the preparation of TiO_2. During the combustion process, the rapid redox reaction between the titanium precursor and the bio-derived fuels generates a large amount of gaseous products, which produces a highly porous nanoparticulate structure with numerous interparticle voids [98]. As a result, the obtained TiO_2 nanoparticles possess a large surface area and well-developed mesoporosity.

The BET analysis reveals a progressive evolution of the textural properties across the composite series. Plasma treatment increases the surface area of carbon nitride by generating structural defects and partial exfoliation, while the incorporation of TiO_2 nanoparticles---particularly those produced via dual combustion synthesis---further enhances the accessible surface area by stabilizing the nanosheet framework and introducing additional mesoporosity. Among the investigated samples, $40TiO_2$/d-g-C_3N_4 exhibits the most favorable textural characteristics, combining a high specific surface area with a large pore volume and a well-developed mesoporous network.

Table 2: Textural properties of the prepared samples

Parameter	**Method**	**g-C3N4**	**d-g-C3N4**	**5TiO2/d-g-C3N4**	**10 TiO2/d-g-C3N4**	**20 TiO2/d-g-C3N4**	**40 TiO2/d-g-C3N4**	**80 TiO2/d-g-C3N4**	**TiO2**
Specific surface area (BET) ($m^2 g^{-1}$)	BET	16.8	27.4	31.2	34.7	38.6	52.1	44.3	63.5
Specific surface area (Langmuir) ($m^2 g^{-1}$)	Langmuir	23.6	36.9	41.8	46.5	51.2	69.4	58.7	82.1
Average particle size (nm)	BET-derived	92.5	61.4	55.8	49.2	43.7	32.6	36.9	27.1
Pore diameter (adsorption) (nm)	BJH	17.6	15.8	15.5	15.2	14.9	13.7	14.1	12.5

Pore diameter (desorption) (nm)	BJH	18.9	16.7	16.3	15.9	15.5	14.2	14.6	13.2
Total pore volume (adsorption) ($cm^3 g^{-1}$)	BJH	0.072	0.103	0.118	0.127	0.136	0.184	0.158	0.211
Total pore volume (desorption) ($cm^3 g^{-1}$)	BJH	0.081	0.118	0.132	0.141	0.148	0.196	0.172	0.226
Isotherm type	IUPAC	IV	IV	IV	IV	IV	IV	IV	IV

II- 6.Photocatalytic Hydrogen Evolution Performance:

The photocatalytic hydrogen evolution performance of the prepared samples under simulated solar irradiation is summarized in Table 3. A clear difference in hydrogen production activity is

observed among the investigated materials, highlighting the crucial roles of defect engineering and heterojunction formation in governing the photocatalytic behavior.

As shown in Table 3, pristine TiO_2 exhibits the lowest hydrogen evolution activity, producing only 0.48 mmol g^{-1} of H_2 after 4 h with an average evolution rate of 0.12 mmol g^{-1} h^{-1}. In contrast, pristine g-C_3N_4 shows a considerably higher activity, reaching 3.63 mmol g^{-1} after 4 h and an average rate of 0.9 mmol g^{-1} h^{-1}, which can be attributed to its narrower band gap and stronger visible-light absorption compared with TiO_2. After plasma treatment, the hydrogen evolution performance further increases for d-g-C_3N_4, which achieves 5.25 mmol g^{-1} of hydrogen after 4 h with an average rate of 1.3 mmol g^{-1} h^{-1}. The enhanced activity confirms that plasma

induced defect sites in carbon nitride improve light harvesting and promote the separation of photogenerated charge carriers [99].

A more pronounced enhancement is observed after coupling d-g-C_3N_4 with TiO_2 to form heterostructured composites. The hydrogen evolution gradually increases from 14.78 mmol g^{-1} for 5TiO_2/d-g-C_3N_4 to 21.22 mmol g^{-1} for 10TiO_2/d-g-C_3N_4, and further to 30.86 mmol g^{-1} for 20TiO_2/d-g-C_3N_4 after 4 h of irradiation. This progressive increase indicates that the incorporation of TiO_2 significantly enhances interfacial charge transfer and effectively suppresses electron--hole recombination [100]. Among all investigated samples, 40TiO_2/d-g-C_3N_4 exhibits the highest photocatalytic activity, producing 35.64 mmol g^{-1} of hydrogen after 4 h with an average hydrogen evolution rate of 8.9 mmol g^{-1} h^{-1}. However, when the TiO_2 content is further increased to 80TiO_2/d-g-C_3N_4, the hydrogen evolution decreases to 27.2 mmol g^{-1} with a rate of 6.8 mmol g^{-1} h^{-1}, indicating that excessive TiO_2 loading becomes unfavorable for photocatalytic performance [101].

The superior activity of 40TiO_2/d-g-C_3N_4 originates from the optimal balance between light absorption, structural accessibility, and interfacial charge separation [102]. Compared with pristine TiO_2, the composite benefits from the strong visible-light absorption of defect-engineered carbon nitride. Meanwhile, compared with pristine g-C_3N_4 and d-g-C_3N_4, the incorporation of TiO_2 forms an efficient heterojunction interface that facilitates directional charge transfer and suppresses recombination [103]. At low TiO_2 loading, the heterojunction effect is present but remains limited due to the insufficient number of TiO_2 domains acting as electron-accepting sites [104]. When the TiO_2 content reaches 40 wt%, the interfacial contact between the two semiconductors becomes well developed, enabling more efficient separation and migration of photogenerated carriers [105]. This

interpretation is fully consistent with the structural, optical, and morphological characterizations discussed in the previous sections.

The UV--vis analysis showed that the composites exhibit extended light absorption and reduced apparent band gap compared with pristine TiO_2, which favors solar-light utilization. The XRD results confirmed that plasma treatment introduces structural disorder into g-C_3N_4, while the addition of TiO_2 restores crystallinity and forms well-defined anatase-containing heterostructures. The SEM observations revealed that the 40TiO_2/d-g-C_3N_4 sample possesses the most balanced morphology, where TiO_2 nanoparticles are densely and uniformly distributed over the defect-engineered carbon nitride nanosheets, ensuring intimate interfacial contact without fully covering the layered structure. In addition, the BET analysis showed that 40TiO_2/d-g-C_3N_4 has the most favorable textural properties among the composite samples, combining high specific surface area and large pore volume, which provide abundant accessible active sites and facilitate reactant diffusion. Therefore, the highest hydrogen evolution observed for this sample results from the synergistic combination of enhanced light absorption, efficient heterojunction formation, high surface accessibility, and improved charge separation [106].

By contrast, the lower activity of 80TiO_2/d-g-C_3N_4 is attributed to excessive TiO_2 coverage. At such high loading, TiO_2 becomes the dominant structural phase, partially masking the visible-light-responsive d-g-C_3N_4 surface and reducing the contribution of defect-rich carbon nitride to the photocatalytic process [107]. Excessive TiO_2 content also promotes particle aggregation, decreases the effective heterojunction quality, and limits the accessibility of active sites. As a result, despite the higher crystallinity of the anatase phase, the overall hydrogen evolution performance decreases [108].

Based on these results, the photocatalytic hydrogen evolution mechanism over the TiO_2/d-g-C_3N_4 heterostructure can be described as follows. Upon solar-light irradiation, the semiconductor absorbs photons and generates electron--hole pairs [109]: Photocatalyst + $h\nu \rightarrow e^-$ (CB) + h^+ (VB)

The photogenerated electrons participate in the hydrogen evolution reaction, reducing water or protons to form molecular hydrogen [110]: $2H_2O + 2e^- \rightarrow H_2 + 2OH^-$ or $2H^+ + 2e^- \rightarrow H_2$

At the same time, the photogenerated holes are consumed by triethanolamine (TEOA), which acts as a sacrificial electron donor and efficiently suppresses charge recombination. The oxidation

of TEOA proceeds through successive steps. First, TEOA is oxidized by photogenerated holes [111]:

$$(HOCH_2CH_2)_3N + h^+ \rightarrow (C_2H_4OH)_2N\text{--}CHO + H^+$$

The intermediate then undergoes further oxidation in the presence of water and additional holes [111]:

$$C_2H_4OH)_2N\text{--}CHO + H_2O + h^+ \rightarrow (C_2H_4OH)_2N\text{--}COOH + 2H^+$$

Finally, the carboxyl-containing intermediate is further oxidized, releasing carbon dioxide and additional protons [111]:

$$(C_2H_4OH)_2N\text{--}COOH + h^+ \rightarrow CO_2 + degraded\ species + H^+$$

Thus, the oxidation of TEOA continuously consumes holes and generates protons, while the photogenerated electrons are utilized for hydrogen production [112]. In the optimized 40TiO_2/d-g-C_3N_4 system, the heterojunction interface promotes efficient separation of photogenerated charges, the defect sites in d-g-C_3N_4 enhance visible-light absorption and carrier trapping, and the TiO_2 nanoparticles provide effective electron-accepting and hydrogen-evolving sites. The cooperative effect of these factors leads to the markedly enhanced photocatalytic hydrogen evolution performance.

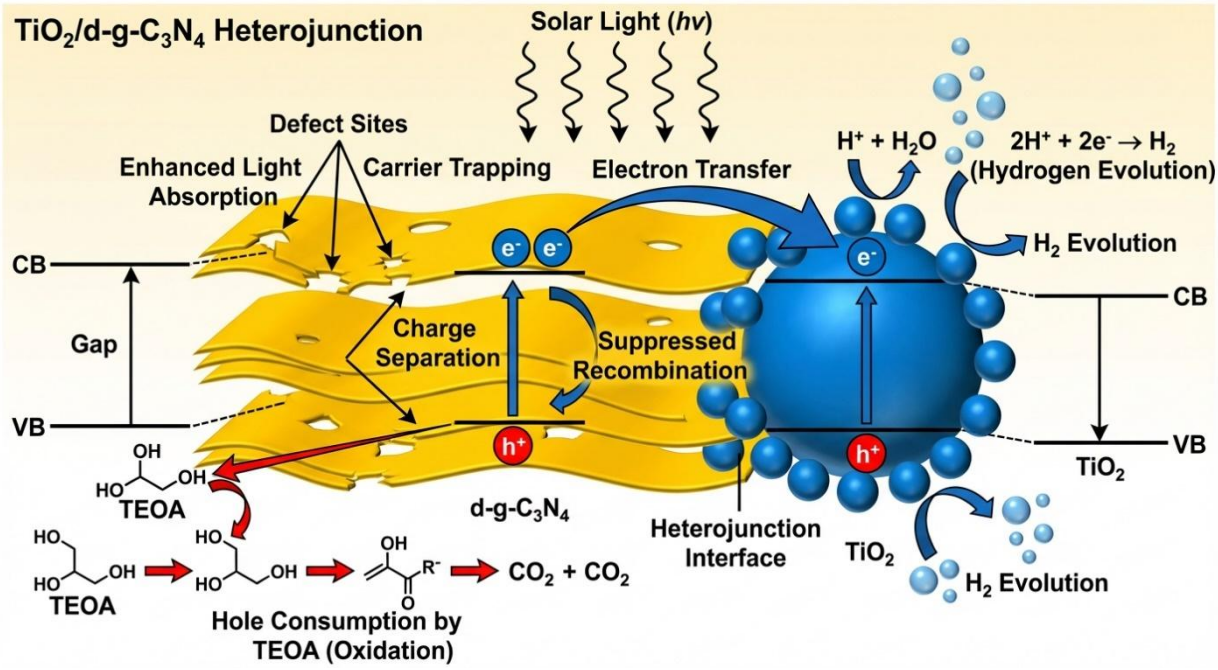

Table 3: Photocatalytic hydrogen evolution performance of the prepared samples

Sample	1 h (mmol g^{-1})	2 h (mmol g^{-1})	3 h (mmol g^{-1})	4 h (mmol g^{-1})	Average rate (mmol g^{-1} h^{-1})
TiO_2	0.11	0.23	0.36	0.48	0.12
g-C_3N_4	0.24	0.60	0.98	3.63	0.9
d-g-C_3N_4	0.38	0.92	1.61	5.25	1.3
5TiO_2/d-g-C_3N_4	0.81	2.47	6.73	14.78	3.7
10TiO_2/d-g-C_3N_4	0.98	3.16	9.3	21.22	5.3
20TiO_2/d-g-C_3N_4	1.26	4.27	12.48	30.86	7.7
40TiO_2/d-g-C_3N_4	1.69	5.13	15.83	35.64	8.9
80TiO_2/d-g-C_3N_4	1.11	4.18	10.03	27.2	6.8

Table 4 compares the hydrogen evolution performance of the present TiO_2/d-g-C_3N_4 photocatalyst with representative TiO_2/g-C_3N_4-based systems reported in recent literature. As shown in the table, the hydrogen evolution activity reported for TiO_2/g-C_3N_4 heterostructures varies widely depending on the heterojunction configuration, defect engineering strategy, and structural architecture. For example, Li et al. reported an S-scheme TiO_2/g-C_3N_4 heterojunction delivering a hydrogen evolution rate of 5.8 mmol g^{-1} h^{-1} [113], while Alsalme et al. achieved 6.8 mmol g^{-1} h^{-1} through composition optimization of TiO_2/g-C_3N_4 S-scheme composites [116]. Similarly, plasmon-assisted Ag@r-TiO_2/g-C_3N_4 heterostructures showed a rate of 6.63 mmol g^{-1} h^{-1} due to enhanced charge transfer and surface plasmon effects [119].

Other structural approaches, such as porous nanotubular g-C_3N_4/TiO_2 architectures and hollow-sphere heterostructures, have also been explored to improve light harvesting and charge separation, achieving hydrogen evolution rates of 4122 μmol g^{-1} h^{-1} and 1200 μmol g^{-1} h^{-1}, respectively [115,117]. In addition, defect engineering has been widely demonstrated as an effective strategy for enhancing photocatalytic activity. For instance, plasma-induced carboxyl-defective g-C_3N_4 loaded with single-atom Cu exhibited 8.34 mmol g^{-1} h^{-1} hydrogen production due to the synergistic effects of defect sites and atomically dispersed catalytic centers [120].

Notably, the 40TiO_2/d-g-C_3N_4 photocatalyst developed in this work exhibits a hydrogen evolution rate of 8.90 mmol g^{-1} h^{-1}, which is higher than most of the previously reported TiO_2/g-C_3N_4 systems listed in Table 4. This superior performance can be attributed to the synergistic combination of plasma-induced defect engineering and optimized TiO_2 loading, which simultaneously enhances visible-light absorption, promotes efficient charge separation at the heterojunction interface, and increases the density of catalytically active sites. The plasma treatment introduces defect sites within the g-C_3N_4 framework that act as electron trapping centers, while the well-distributed TiO_2 nanoparticles provide efficient electron-accepting and hydrogen evolution sites. Consequently, the optimized heterostructure achieves efficient interfacial charge transfer and significantly improved photocatalytic hydrogen evolution performance.

Table 4: Comparison of hydrogen evolution performance with previously reported TiO2/g-C3N4 photocatalysts

Sample / Photocatalyst	H2 evolution rate	Reference

TiO2/g-C3N4 S-scheme heterojunction	5.8 mmol g-1 h-1	[113]
OVs-TiO2/g-C3N4 heterojunction	150 umol h-1	[114]
Porous nanotubular g-C3N4/TiO2 Z-scheme	4122 umol g-1 h-1	[115]
TiO2/g-C3N4 S-scheme composite	6.8 mmol g-1 h-1	[116]
g-C3N4/TiO2 hollow spheres	1200 umol g-1 h-1	[117]
Ni single-atom TiO2/g-C3N4	134 umol g-1 h-1	[118]
Ag@r-TiO2/g-C3N4 heterostructure	6.63 mmol g-1 h-1	[119]
Plasma-defective Cu/g-C3N4	8.34 mmol g-1 h-1	[120]
40TiO2/d-g-C3N4 (This work)	8.90 mmol g-1 h-1	This work

II-7. Active Species Trapping Experiments:

To clarify the dominant reactive species involved in the photocatalytic hydrogen evolution process, trapping experiments were carried out using different scavengers, and the results are summarized in Table 5. In general, the introduction of IPA, BQ, and EDTA caused different extents of activity suppression depending on the role of the corresponding reactive species in the photocatalytic process.

For all samples, the addition of IPA, used as a scavenger for hydroxyl radicals (•OH), leads only to a slight decrease in hydrogen evolution activity. For example, the hydrogen evolution rate of $40TiO_2/d\text{-}g\text{-}C_3N_4$ decreases from 8.90 to 8.30 mmol g^{-1} h^{-1}, while that of $20TiO_2/d\text{-}g\text{-}C_3N_4$ decreases from 7.70 to 7.20 mmol g^{-1} h^{-1}. A similarly small reduction is observed for the other samples. This weak influence indicates that hydroxyl radicals do not play a major role in the

hydrogen evolution pathway. Instead, the photocatalytic process is dominated by charge-carrier-driven reduction reactions rather than oxidative radical reactions involving •OH species.

In contrast, the addition of BQ, which acts as a scavenger for superoxide radicals ($O_2^{\bullet -}$), results in a pronounced decrease in hydrogen production for all samples. The activity of 40TiO_2/d-g-C_3N_4 decreases sharply from 8.90 to 5.10 mmol g^{-1} h^{-1}, while 20TiO_2/d-g-C_3N_4 drops from 7.70 to 4.65 mmol g^{-1} h^{-1}, and 10TiO_2/d-g-C_3N_4 decreases from 5.30 to 3.32 mmol g^{-1} h^{-1}. The same trend is observed for pristine g-C_3N_4, d-g-C_3N_4, and TiO_2. This significant suppression confirms that electron-related reduction pathways are essential in the photocatalytic hydrogen evolution process, and that $O_2^{\bullet -}$-associated charge transfer is strongly involved in the reaction system [121]. The strong sensitivity to BQ clearly demonstrates that the preservation and migration of photogenerated electrons are crucial for sustaining high hydrogen production [122].

The effect of EDTA, used as a hole scavenger (h^+), is different from that of IPA and BQ. For some samples, the addition of EDTA leads to a slight increase or near-retention of activity. This is especially evident for 10TiO_2/d-g-C_3N_4, whose hydrogen evolution rate increases from 5.30 to 6.10 mmol g^{-1} h^{-1}, and for 40TiO_2/d-g-C_3N_4, which slightly increases from 8.90 to 9.40 mmol g^{-1} h^{-1}. Likewise, 20TiO_2/d-g-C_3N_4 is almost unchanged, increasing slightly from 7.70 to 7.72 mmol g^{-1} h^{-1}, while 80TiO_2/d-g-C_3N_4 increases from 6.80 to 6.95 mmol g^{-1} h^{-1}. This behavior indicates that the consumption of photogenerated holes is beneficial for the photocatalytic system because it suppresses electron--hole recombination and allows a larger number of electrons to participate in proton reduction [123]. For samples such as TiO_2 and g-C_3N_4, the change upon EDTA addition remains limited, suggesting that the hole-removal effect is more pronounced in the optimized heterojunction systems where charge separation is already more efficient.

Among all samples, 40TiO_2/d-g-C_3N_4 remains the most active under all trapping conditions, which further confirms that this composition provides the most efficient interfacial charge-transfer network. The highest control activity, combined with the strongest sensitivity to BQ and the slight enhancement in the presence of EDTA, indicates that this sample achieves the most effective separation of photogenerated charge carriers, where electrons are efficiently utilized for hydrogen evolution while holes are readily consumed by the sacrificial pathway [124].

The scavenger experiments demonstrate that photogenerated electrons are the dominant active species responsible for hydrogen evolution, whereas holes mainly participate in the oxidation of the sacrificial reagent and their removal favors charge separation. The minimal influence of IPA

confirms the negligible role of •OH radicals, while the strong suppression caused by BQ identifies the electron-mediated reduction pathway as the key step controlling photocatalytic hydrogen generation [125]. These findings are fully consistent with the superior hydrogen evolution performance of the 40TiO_2/d-g-C_3N_4 heterostructure and support the proposed mechanism of efficient interfacial charge separation in the optimized composite.

Table 5: Radical scavenger experiments for identifying the active species during photocatalytic hydrogen evolution.

Sample	Control (mmol g^{-1} h^{-1})	+IPA (•OH)	+BQ (O_2•$^-$)	+EDTA (h^+)
TiO_2	0.12	0.11	0.08	0.11
g-C_3N_4	0.90	0.87	0.62	0.96
d-g-C_3N_4	1.30	1.25	0.88	1.44
5TiO_2/d-g-C_3N_4	3.70	3.55	2.41	3.65
10TiO_2/d-g-C_3N_4	5.30	5.05	3.32	6.1
20TiO_2/d-g-C_3N_4	7.70	7.20	4.65	7.72
40TiO_2/d-g-C_3N_4	8.90	8.30	5.10	9.4
80TiO_2/d-g-C_3N_4	6.80	6.35	3.95	6.95

II- 8.Recyclability and Stability Test:

The operational stability of the prepared photocatalysts was evaluated through five consecutive photocatalytic hydrogen evolution cycles, and the results are summarized in Table 6. In general, all

samples exhibit relatively stable hydrogen evolution performance over repeated cycles, indicating that the photocatalysts maintain their structural integrity under prolonged irradiation conditions.

For pristine TiO_2, a gradual decrease in activity is observed from 0.12 mmol g^{-1} h^{-1} in the first cycle to 0.08 mmol g^{-1} h^{-1} in the fifth cycle, corresponding to a noticeable loss of catalytic efficiency. This decline is mainly attributed to the limited visible-light absorption of TiO_2 and the higher recombination rate of photogenerated charge carriers, which also affects its long-term photocatalytic stability [126].

In contrast, g-C_3N_4 demonstrates improved stability compared with TiO_2. The hydrogen evolution rate decreases slightly from 0.90 to 0.81 mmol g^{-1} h^{-1} after five cycles, indicating that the polymeric carbon nitride structure remains relatively stable under the reaction conditions. The defect-engineered carbon nitride (d-g-C_3N_4) exhibits even better durability, maintaining 1.20 mmol g^{-1} h^{-1} in the fifth cycle compared with 1.30 mmol g^{-1} h^{-1} in the first cycle. The improved stability can be attributed to the presence of plasma-induced defect sites, which facilitate charge carrier migration and reduce recombination during repeated photocatalytic cycles [127].

A further improvement in recyclability is observed for the TiO_2/d-g-C_3N_4 heterostructured composites. For instance, the activity of 5TiO_2/d-g-C_3N_4 decreases slightly from 3.70 to 3.44 mmol g^{-1} h^{-1} after five cycles, while 10TiO_2/d-g-C_3N_4 retains 4.98 mmol g^{-1} h^{-1} compared with the initial 5.30 mmol g^{-1} h^{-1}. Similarly, 20TiO_2/d-g-C_3N_4 maintains 7.42 mmol g^{-1} h^{-1} after the fifth cycle, demonstrating that the introduction of TiO_2 significantly enhances the structural robustness and operational stability of the photocatalyst [128].

Among all samples, 40TiO_2/d-g-C_3N_4 exhibits the best stability and recyclability. The hydrogen evolution rate decreases only slightly from 8.90 to 8.63 mmol g^{-1} h^{-1} after five cycles, corresponding to a retention of approximately 97% of the initial activity. This excellent durability confirms the strong interfacial interaction between TiO_2 nanoparticles and defect-engineered carbon nitride nanosheets, which ensures efficient charge transfer and prevents structural degradation during repeated photocatalytic reactions [129].

When the TiO_2 loading is further increased to 80TiO_2/d-g-C_3N_4, the activity remains relatively stable but slightly lower than that of the optimal composition, decreasing from 6.80 to 6.47 mmol g^{-1} h^{-1} after five cycles. This behavior suggests that excessive TiO_2 loading does not significantly

improve structural stability and may partially reduce the contribution of the carbon nitride component to the photocatalytic process [130].

The recyclability results demonstrate that the TiO_2/d-g-C_3N_4 heterostructures possess excellent operational stability, particularly for the optimized 40TiO_2/d-g-C_3N_4 composition. The minimal loss in activity after five cycles confirms the robustness of the heterojunction structure and highlights the potential of this material for long-term photocatalytic hydrogen production.

Table 6: Recyclability test of photocatalytic hydrogen evolution for five consecutive cycles

Sample	**Cycle 1 (mmol g^{-1} h^{-1})**	**Cycle 2**	**Cycle 3**	**Cycle 4**	**Cycle 5**
TiO_2	0.12	0.12	0.11	0.09	0.08
g-C_3N_4	0.90	0.88	0.86	0.82	0.81
d-g-C_3N_4	1.30	1.27	1.25	1.21	1.20
5TiO_2/d-g-C_3N_4	3.70	3.64	3.59	3.52	3.44
10TiO_2/d-g-C_3N_4	5.30	5.26	5.17	5.09	4.98
20TiO_2/d-g-C_3N_4	7.70	7.64	7.56	7.50	7.42
40TiO_2/d-g-C_3N_4	8.90	8.88	8.75	8.72	8.63
80TiO_2/d-g-C_3N_4	6.80	6.70	6.63	6.55	6.47

II - 9.Photoelectrochemical Performance:

The transient photocurrent responses of the prepared samples are shown in Figure 5. The photocurrent density reflects the efficiency of photogenerated charge separation and transport within the photocatalyst system. As observed in the figure, all samples exhibit stable and reproducible photocurrent signals during repeated light on--off cycles, indicating rapid photoresponse and good photoelectrochemical stability.

Pristine TiO_2 exhibits the lowest photocurrent density of approximately 0.12 μA cm^{-2}, which is mainly attributed to its limited visible-light absorption and the fast recombination of photogenerated electron--hole pairs. In contrast, g-C_3N_4 shows a higher photocurrent response of about 0.35 μA cm^{-2}, owing to its narrower band gap and stronger visible-light absorption [131].

After plasma treatment, the photocurrent density further increases for d-g-C_3N_4 to approximately 0.55 μA cm^{-2}, indicating that the introduced defect sites improve charge carrier migration and suppress recombination. These defect states act as electron trapping centers that enhance the separation efficiency of photogenerated charge carriers [132].

A significant enhancement is observed after forming the TiO_2/d-g-C_3N_4 heterostructures. The photocurrent density gradually increases from 0.95 μA cm^{-2} for 5TiO_2/d-g-C_3N_4 to 1.65 μA cm^{-2} for 20TiO_2/d-g-C_3N_4, reaching a maximum value of approximately 2.05 μA cm^{-2} for 40TiO_2/d-g-C_3N_4. This progressive improvement demonstrates that the heterojunction formation significantly enhances interfacial charge transfer and suppresses electron--hole recombination [133].

When the TiO_2 loading increases further to 80TiO_2/d-g-C_3N_4, the photocurrent density slightly decreases to about 1.70 μA cm^{-2}, suggesting that excessive TiO_2 may partially cover the active carbon nitride surface and reduce the contribution of the visible-light-responsive component [134].

The highest photocurrent response observed for 40TiO_2/d-g-C_3N_4 confirms that this composition provides the most efficient charge separation and transfer pathway, which is consistent with its superior photocatalytic hydrogen evolution performance.

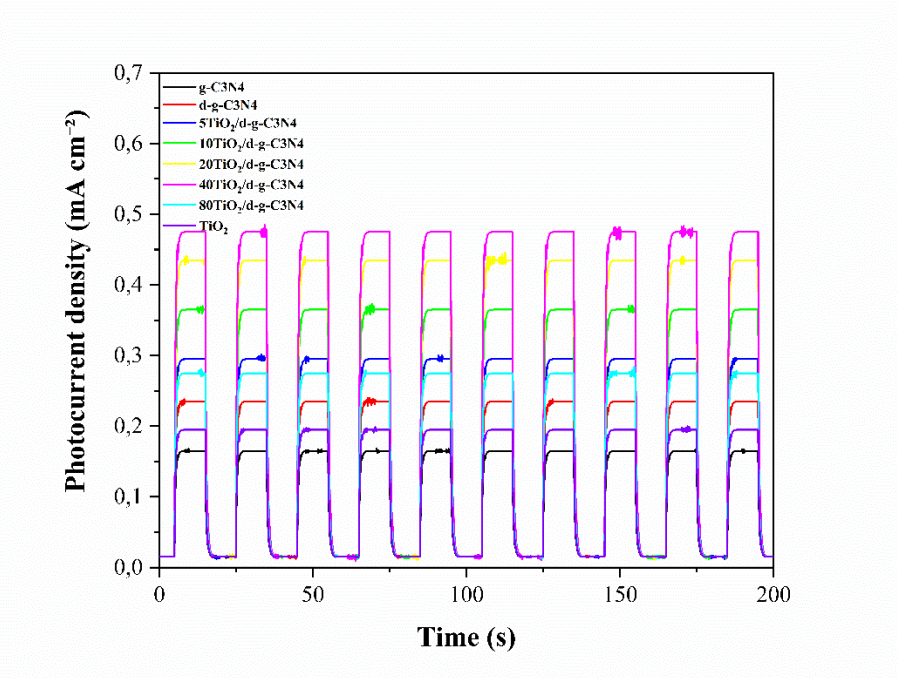

Figure 18: Transient photocurrent response of pure TiO2, g-C3N4, d-g-C3N4, and TiO2/d-g-C3N4 nanocomposites with different weight ratio

Conclusion

Conclusion:

A defect-regulated TiO_2/d-g-C_3N_4 heterojunction photocatalyst was successfully developed through the combination of plasma-induced defect engineering and green bio-combustion synthesis. Plasma treatment introduced structural defects into g-C_3N_4, improving light absorption and charge carrier migration, while the TiO_2 nanoparticles formed an efficient heterojunction interface that enhances charge separation.

The optimized 40TiO_2/d-g-C_3N_4 sample exhibited the highest photocatalytic hydrogen evolution rate of 8.9 mmol g^{-1} h^{-1} along with excellent stability. The superior performance arises from the synergistic interaction between defect sites and the heterojunction interface, which increases active sites and accelerates interfacial electron transfer.

This work demonstrates an effective strategy for designing high-performance photocatalysts through the integration of defect engineering, heterojunction construction, and sustainable synthesis, providing a promising approach for solar-driven hydrogen production.

References

References :

[1]Kumar, Niraj, et al. "Recent progress in catalysts for sustainable hydrogen production: A comprehensive review." Coordination Chemistry Reviews 547 (2026): 217109.

[2]Hisatomi, Takashi, Jun Kubota, and Kazunari Domen. "Recent advances in semiconductors for photocatalytic and photoelectrochemical water splitting." Chemical Society Reviews 43.22 (2014): 7520-7535.

[3]Sano, Keito, et al. "To the next stage of artificial photosynthesis by molecular catalysts: transparent aqueous dispersion of semiconductor nanoparticles." Research on Chemical Intermediates (2026): 1-31.

[4]Radhakrishnan, Sruthi, et al. "Biological and Environmental Applications of Myco-synthesized Titanium Dioxide Nanoparticles." BioNanoScience 16.1 (2026): 31.

[5]Schneider, Jenny, et al. "Understanding TiO2 photocatalysis: mechanisms and materials." Chemical reviews 114.19 (2014): 9919-9986.

[6]Low, Jingxiang, et al. "Heterojunction photocatalysts." Advanced materials 29.20 (2017): 1601694.

[7]Ong, Wee-Jun, et al. "Graphitic carbon nitride (g-C3N4)-based photocatalysts for artificial photosynthesis and environmental remediation: are we a step closer to achieving sustainability?." Chemical reviews 116.12 (2016): 7159-7329.

[8]Wang, Xinchen, et al. "A metal-free polymeric photocatalyst for hydrogen production from water under visible light." Nature materials 8.1 (2009): 76-80.

[9]Zhang, Jinshui, et al. "A facile band alignment of polymeric carbon nitride semiconductors to construct isotype heterojunctions." Angewandte Chemie 124.40 (2012): 10292-10296.

[10]Wang, Yong, Xinchen Wang, and Markus Antonietti. "Polymeric graphitic carbon nitride as a heterogeneous organocatalyst: from photochemistry to multipurpose catalysis to sustainable chemistry." Angewandte Chemie International Edition 51.1 (2012): 68-89.

[11]Gong, Eunhee, et al. "Revealing the structure-activity relationship of Mn3O4/TiO2 via phase engineering for enhanced photocatalytic CO_2 reduction." Journal of CO2 Utilization 105 (2026): 103357.

[12]Mohammaddarvish, Samira, Amir Ali Masoudi, and Zahra Sadat Hosseini. "Boosting visible-light photocatalysis with MWCNT-modified TiO2/SiO2/g-C3N4: efficient tetracycline removal in pure and hard water." Scientific Reports (2026).

[13]Chau, Ngoc Hoang, et al. "Printable TiO_2@ g-C_3N_4 photoelectrodes for efficient water splitting." Electrochimica Acta (2025): 148071.

[14]Ren, Haitao, et al. "Coordination engineering in dual S-scheme heterojunction for photocatalytic applications: Research progress, key challenges and future horizons." Coordination Chemistry Reviews 548 (2026): 217183.

[15] Revue Recherches qualitatives (2009). Vol. 28(1), Numéro spécial "L'analyse qualitative des données". ISSN 1715-8702.

[16] Terea, H., Selloum, D., Rebiai, A., Atia, D., Kouadri, I., Ben Seghir, B., & Messaoudi, M. (2023b). Characterization, biological, and antimicrobial properties of nanocellulose isolated from peanut shells (Arachis hypogaea L.). Biomass Conversion and Biorefinery. https://doi.org/10.1007/s13399-023-04792-8

[17] Kayet, A. (2020). Outils et techniques d'analyse des données. Editions Notre Savoir. ISBN 9786202866019.

[18] Laraoui, N. (2020/2021). Cours de Techniques de recherche (3ème année licence). Université Frères Mentouri Constantine 1.

[19] Corbière, M., & Larivière, N. (Eds.). (2014). Méthodes qualitatives, quantitatives et mixtes: Dans la recherche en sciences humaines, sociales et de la santé. Presses de l'Université du Québec.

[20] Terea, H. (2023). Application of cellulose/ZnO nanocomposite on the removal of toxic pollutants from aqueous solutions (Thèse de doctorat). University of Kasdi Merbah -- Ouargla, Algeria.

[21] Lowell, S., Shields, J. E., Thomas, M. A., & Thommes, M. (2004). Characterization of Porous Solids and Powders: Surface Area, Pore Size and Density. Springer.

[22] Brunauer, S., Emmett, P. H., & Teller, E. (1938). Adsorption of gases in multimolecular layers. Journal of the American Chemical Society, 60(2), 309--319.

[23] Guillemette, F., & Berthiaume, M.-J. (2015). Listes de références sur la recherche qualitative (version 2015). Sur plateforme Erudit, ISSN 2292-0005.

[24] Guillemette, F. (2008). Bibliographie sur l'analyse qualitative. Recherches Qualitatives, (10), 1-16. ISSN 1715-8702.

[25] Terea, H., Selloum, D., Rebiai, A., Bouafia, A., & Ben Mya, O. (2023a). Preparation and characterization of cellulose/ZnO nanoparticles extracted from peanut shells: Effects on antibacterial and antifungal activities. Biomass Conversion and Biorefinery. https://doi.org/10.1007/s13399-023-03959-7

[26] Thommes, M., Kaneko, K., Neimark, A. V., Olivier, J. P., Rodriguez-Reinoso, F., Rouquerol, J., & Sing, K. S. W. (2015). Physisorption of gases, with special reference to the evaluation of surface area and pore size distribution (IUPAC Technical Report). Pure and Applied Chemistry, 87(9-10), 1051-1069.

[27] Hoffmann, M. R., Martin, S. T., Choi, W., & Bahnemann, D. W. (1995). Environmental applications of semiconductor photocatalysis. Chemical Reviews, 95(1), 69-96.

[28] Wang, X., Blechert, S., & Antonietti, M. (2012). Polymeric graphitic carbon nitride for heterogeneous photocatalysis. ACS Catalysis, 2(8), 1596-1606.

[29] Schneider, J., Matsuoka, M., Takeuchi, M., Zhang, J., Horiuchi, Y., Anpo, M., & Bahnemann, D. W. (2014). Understanding TiO_2 photocatalysis: mechanisms and materials. Chemical Reviews, 114(19), 9919-9986.

[30] Ong, W. J., Tan, L. L., Ng, Y. H., Yong, S. T., & Chai, S. P. (2016). Graphitic carbon nitride ($g\text{-}C_3N_4$)-based photocatalysts for artificial photosynthesis and environmental remediation: Are we a step closer to achieving sustainability? Chemical Reviews, 116(12), 7159-7329.

[31] Fujishima, A., Zhang, X., & Tryk, D. A. (2008). TiO_2 photocatalysis and related surface phenomena. Surface Science Reports, 63(12), 515-582.

[32] Linsebigler, A. L., Lu, G., & Yates, J. T. (1995). Photocatalysis on TiO_2 surfaces: principles, mechanisms, and selected results. Chemical Reviews, 95(3), 735-758.

[33] Kudo, A., & Miseki, Y. (2009). Heterogeneous photocatalyst materials for water splitting. Chemical Society Reviews, 38(1), 253-278.

[34] Zhang, J., Chen, Y., & Wang, X. (2015). Two-dimensional covalent carbon nitride nanosheets: synthesis, functionalization, and applications. Energy & Environmental Science, 8(11), 3092-3108.

[35] Pelaez, M., Nolan, N. T., Pillai, S. C., Seery, M. K., Falaras, P., Kontos, A. G., ... & Dionysiou, D. D. (2012). A review on the visible light active titanium dioxide photocatalysts for environmental applications. Applied Catalysis B: Environmental, 125, 331-349.

[36] Li, X., Yu, J., & Jaronec, M. (2016). Hierarchical photocatalysts. Chemical Society Reviews, 45(9), 2603-2636.

[37] Yao et al. (2020). Photocatalytic Reforming for Hydrogen Evolution: A Comprehensive Review of Recent Advances and Challenges. Catalysts.

[38] Chen et al. (2010). Semiconductor-Based Photocatalytic Hydrogen Generation. Chemical Reviews.

[39] Acar et al. (2016). A Review on Selected Aspects of Photocatalytic Water Splitting for Hydrogen Production. International Journal of Energy Research.

[40] Ni et al. (2007). A Review and Recent Developments in Photocatalytic Water Splitting Using TiO_2. Renewable and Sustainable Energy Reviews.

[41] Wang & Domen (2020). Photocatalysts for Water Splitting. Chemical Reviews.

[42] Dawood et al. (2020). Hydrogen Production for Energy: An Overview. International Journal of Hydrogen Energy.

[43] Nikolaidis & Poullikkas (2017). Hydrogen Production Processes Overview. Renewable and Sustainable Energy Reviews.

[44] Carmo et al. (2013). PEM Water Electrolysis Review. International Journal of Hydrogen Energy.

[45] Laguna-Bercero (2012). Solid Oxide Electrolysis for Hydrogen Production. Journal of Power Sources.

[46] Armor (1999). Catalysis in Hydrogen Production. Applied Catalysis A.

[47] Khelfaoui, Trili, Areig (2020). Green Hydrogen: Production Technologies and Energy Applications. Master's Thesis.

[48] Steinfeld (2005). Solar Thermochemical Hydrogen Production. Solar Energy.

[49] Das & Veziroğlu (2001). Biological Hydrogen Production. International Journal of Hydrogen Energy.

[50] Balarabe et al. (2026). Photoelectrochemical Hydrogen Production Advances. Discover Nano.

[51] Ong et al. (2016). Graphitic Carbon Nitride-Based Photocatalysts. Chemical Reviews.

[52] Turner (2004). Sustainable Hydrogen Production. Science.

[53] Zhang, X., & Jiang, S. P. (2022). Layered g-C_3N_4/TiO_2 nanocomposites for efficient photocatalytic water splitting and CO_2 reduction: a review. Materials Today Energy, 23, 100904.

[54] Chen, X., & Mao, S. S. (2024). Recent Advances in TiO_2-Based Photocatalysts for Efficient Water Splitting to Hydrogen. International Journal of Hydrogen Energy.

[55] Serna, F., J. Lagneau, and J.-M. Carpentier, La diffraction des rayons X: une technique puissante pour résoudre certains problèmes industriels et technologiques. Chim. Nouv, 2014: p. 1-12.

[56] Ghidan, A.Y., T.M. Al-Antary, and A.M. Awwad, Green synthesis of copper oxide nanoparticles using Punica granatum peels extract: Effect on green peach Aphid. Environmental Nanotechnology, Monitoring & Management, 2016. 6: p. 95-98.

[57] Megashah, L.N., et al., Modification of cellulose degree of polymerization by superheated steam treatment for versatile properties of cellulose nanofibril film. Cellulose, 2020. 27(13): p. 7417-7429.

[58] PAQUETON, H. and J. RUSTE, Microscopie électronique à balayage Principe et équipement. Techniques de l'ingénieur. Analyse et caractérisation, 2006(P865v2).

[59] Ben Mya, O., Synthèse et caractérisation de la pérovskite La1-x SrxFe0.7Ni0.3O3. 2015, Université Mohamed Khider-Biskra.

[60] Inkson, B.J., Scanning electron microscopy (SEM) and transmission electron microscopy (TEM) for materials characterization, in Materials characterization using nondestructive evaluation (NDE) methods. 2016, Elsevier. p. 17-43.

[61] George, G., R. Wilson, and J. Joy, Ultraviolet Spectroscopy: A Facile Approach for the Characterization of Nanomaterials, in Spectroscopic Methods for Nanomaterials Characterization. 2017, Elsevier. p. 55-72.

[62] Mäntele, W. and E. Deniz, UV--VIS absorption spectroscopy: Lambert-Beer reloaded. 2017, Elsevier. p. 965-968.

[63] Tauc, J. and A. Menth, States in the gap. Journal of non-crystalline solids, 1972. 8: p. 569-585.

[64] De Viguerie, L., Propriétés physico-chimiques et caractérisation des matériaux du 'sfumato'. 2009, Université Pierre et Marie Curie-Paris VI.

[65] GUERRAM, A., Synthèse verte et caractérisation des nanoparticules de ZnO à l'aide d'extrait des feuilles de Phoenix dactylifera L et leur applications. 2022, Faculté des Sciences et de la technologie.

[66] Luo, Tong, et al. "Controllable fabrication of high-performance porous cage-like CaO microspheres by dual-fluid spray combustion synthesis for thermochemical energy storage." Separation and Purification Technology (2025): 134400.

[67] Ndiaye, Diop, and Arjun Akill. "A critical review on g-C_3N_4 for environmental remediation: synthesis, properties, and pollutant photodegradation." Rendiconti Lincei. Scienze Fisiche e Naturali (2025): 1-25.

[68] Xiang, Quanjun, et al. "Plasma-based surface modification of g-C3N4 nanosheets for highly efficient photocatalytic hydrogen evolution." Applied Surface Science 495 (2019): 143520.

[69] Ding, Jianjun, et al. "Plasma synthesis of Pt/g-C3N4 photocatalysts with enhanced photocatalytic hydrogen generation." Journal of Alloys and Compounds 873 (2021): 159871.

[70] Gaidukevič, Justina, et al. "Study on the structure and electrocatalytic activity of graphene-based nanocomposite materials containing (SCN) n." Carbon 118 (2017): 156-167.

[71] Aouadi, Abdelatif, et al. "Defect-engineered MgO nanoparticles with high surface area for integrated solar-driven CO2 reduction and hydrogen generation." Ionics (2026): 1-19.

[72] Soltaninezhad, Fatemeh, and Fariba Fathirad. "Synthesis and characterization of g-C_3N_4/$BiVO_4$ nanosheets: Exploring the effect of doping and heterostructure coupling on photoelectrochemical performance." Diamond and Related Materials (2025): 112760.

[73] Schneider, Jenny, et al. "Understanding TiO2 photocatalysis: mechanisms and materials." Chemical reviews 114.19 (2014): 9919-9986.

[74] Wang, Xinchen, et al. "A metal-free polymeric photocatalyst for hydrogen production from water under visible light." Nature materials 8.1 (2009): 76-80.

[75] Wen, Dongxiao, et al. "Nitrogen/oxygen dual-defects modified gC 3 N 4 nanosheets for boosting photocatalytic CO 2 reduction." Nano Research 19.1 (2026): 94907945.

[76] Xu, Quanlong, et al. "S-scheme heterojunction photocatalyst." Chem 6.7 (2020): 1543-1559.

[77] Wang, Xinchen, et al. "A metal-free polymeric photocatalyst for hydrogen production from water under visible light." Nature materials 8.1 (2009): 76-80.

[78] Ong, Wee-Jun, et al. "Graphitic carbon nitride (g-C3N4)-based photocatalysts for artificial photosynthesis and environmental remediation: are we a step closer to achieving sustainability?." Chemical reviews 116.12 (2016): 7159-7329.

[79] Thi, Lan Nguyen, et al. "Activated carbon/g-C_3N_4/H_2O_2 system with enhanced photocatalytic activity for Rhodamine-B degradation under the visible light." Environmental Engineering Research 30.1 (2025): 115-131.

[80] Chen, Xiaobo, and Samuel S. Mao. "Titanium dioxide nanomaterials: synthesis, properties, modifications, and applications." Chemical reviews 107.7 (2007): 2891-2959.

[81] Ahamed, M. E. H., and Kriveshini Pillay. "Adsorption of Pb2+ ion using coal fly ash/g-C3N4/Bi2O2CO3 and re-use of spent adsorbent for photocatalytic and forensic applications." (2026).

[82] Ong, Wee-Jun, et al. "Graphitic carbon nitride (g-C3N4)-based photocatalysts for artificial photosynthesis and environmental remediation: are we a step closer to achieving sustainability?." Chemical reviews 116.12 (2016): 7159-7329.

[83] Zhang, Jinshui, et al. "Sol processing of conjugated carbon nitride powders for thin-film fabrication." Angewandte Chemie International Edition 54.21 (2015): 6297-6301.

[84] Li, Xin, et al. "Engineering heterogeneous semiconductors for solar water splitting." Journal of Materials Chemistry A 3.6 (2015): 2485-2534.

[85] Wen, Dongxiao, et al. "Nitrogen/oxygen dual-defects modified gC 3 N 4 nanosheets for boosting photocatalytic CO 2 reduction." Nano Research 19.1 (2026): 94907945.

[86] Xu, Quanlong, et al. "Direct Z-scheme photocatalysts: Principles, synthesis, and applications." Materials Today 21.10 (2018): 1042-1063.

[87] Zolotoyabko, Emil. Basic concepts of X-ray diffraction. John Wiley & Sons, 2014.

[88] Miljak, Marcus AP, Pramod Koshy, and Joel N. O'Dwyer. "Powder X-ray Diffraction Implementation in Geant4." Nuclear Instruments and Methods in Physics Research Section A: Accelerators, Spectrometers, Detectors and Associated Equipment (2026): 171280.

[89] Martinelli, Alberto. "Extending the Williamson-Hall method: a qualitative approach for microstructural analysis under non-ideal conditions." Zeitschrift für Kristallographie-Crystalline Materials 0 (2026).

[90] Şahbaz, Mehmet, and Sinan Nalkıran. "Microstructural refinement and mechanical property enhancement of AZ91 magnesium alloy via room-temperature multi-directional forging." Scientific Reports (2026).

[91] Podagatlapalli, G. Krishna, et al. "Single-beam femtosecond Z-scan studies of bismuth and manganese co-doped titanium dioxide nanoparticles dispersed in ethanol." RSC advances 16.12 (2026): 11023-11035.

[92] Mecchia, Marco, et al. "Quantitative X-ray diffraction analysis of quartz in bulk samples: outcomes of an international interlaboratory test on three standardized methods." Annals of Work Exposures and Health 70.2 (2026): wxaf084.

[93] Hoang, Lan-Anh T., et al. "High-efficiency photocatalytic inactivation of algae using Ag/g-C_3N_4-coated polyurethane filters with enhanced stability and reusability." Materials Science and Engineering: B 327 (2026): 119299.

[94] Chen, Meixuan, et al. "Enhanced Electro-Fenton Performance by ng-C3N4 Modified Carbon Nanotubes for Removal of Organic Pollutants in Wastewater." Water, Air, & Soil Pollution 237.10 (2026): 582.

[95] Počuča-Nešić, Milica, et al. "Porous-Architecture-Driven Performance of Electrospun SnO2 Nanofibers for Reliable H2S Detection." Chemosensors 14.2 (2026): 32.

[96] Low, Jingxiang, et al. "Heterojunction photocatalysts." Advanced materials 29.20 (2017): 1601694.

[97] Ong, Wee-Jun, et al. "Graphitic carbon nitride (g-C3N4)-based photocatalysts for artificial photosynthesis and environmental remediation: are we a step closer to achieving sustainability?." Chemical reviews 116.12 (2016): 7159-7329.

[98] Solution Combustion Synthesis of Nanoscale Materials.

[99] Liu, Li, et al. "Efficient visible-light photocatalytic hydrogen evolution and enhanced photostability of core@ shell Cu2O@ g-C3N4 octahedra." Applied Surface Science 351 (2015): 1146-1154.

[100] Low, Jingxiang, et al. "Heterojunction photocatalysts." Advanced materials 29.20 (2017): 1601694.

[101] Ong, Wee-Jun, et al. "Graphitic carbon nitride (g-C3N4)-based photocatalysts for artificial photosynthesis and environmental remediation: are we a step closer to achieving sustainability?." Chemical reviews 116.12 (2016): 7159-7329.

[102] Li, Huixia, et al. "Pyridine and carbon co-modified carbon nitride for synergistic photocatalytic hydrogen production and pollutant degradation." Materials Research Bulletin (2026): 113998.

[103] Le, Thi Chung, et al. "Engineering Phosphorus Doping Graphitic Carbon Nitride for Efficient Visible-Light Photocatalytic Hydrogen Production." Catalysts 16.1 (2026): 88.

[104] Sinambela, Nelly Christina, et al. "GREEN SYNTHESIS AND CHARACTERIZATION OF TiO2 NANOPARTICLES USING BIO-WASTE EXTRACTS FOR PARACETAMOL PHOTODEGRADATION." Journal of Chemical Technology and Metallurgy 61.2 (2026): 215-224.

[105] Shuaib, Suhaib Shuaib Adam, et al. "Ti3C2 MXene-derived TiO2/g-C3N4 heterojunctions for highly efficient photocatalytic H2 generation." ChemCatChem 17.7 (2025): e202402152.

[106] Li, Xin, et al. "Engineering heterogeneous semiconductors for solar water splitting." Journal of Materials Chemistry A 3.6 (2015): 2485-2534.

[107] Liu, Guigao, et al. "Nature-inspired environmental "phosphorylation" boosts photocatalytic H2 production over carbon nitride nanosheets under visible-light irradiation." Angewandte Chemie International Edition 54.46 (2015): 13561-13565.

[108] Acharya, Krishna P., Mikhail Zamkov, and Jiamin Huang. "Advances in Colloidal InP-Based Quantum Dots for Photocatalytic Hydrogen Evolution." ACS omega (2026).

[109] Sano, Keito, et al. "To the next stage of artificial photosynthesis by molecular catalysts: transparent aqueous dispersion of semiconductor nanoparticles." Research on Chemical Intermediates (2026): 1-31.

[110] Khan, Afsar, and Mustafa Ersoz. "Unveiling the photocatalyst surface poisoning during water splitting: mechanisms, theoretical modeling and anti-poisoning strategies." Catalysis Science & Technology (2026).

[111] Zhu, Kaixin, and Hefeng Zhang. "Recent Advances in Photoelectrochemical Nitrate Reduction to Ammonia." International Journal of Molecular Sciences 27.1 (2026): 470.

[112] Wang, Qian, and Kazunari Domen. "Particulate photocatalysts for light-driven water splitting: mechanisms, challenges, and design strategies." Chemical Reviews 120.2 (2019): 919-985.

[113] Li, Rui, et al. "Fabrication of TiO2/g-C3N4 S-scheme heterojunction photocatalysts for efficient hydrogen evolution." Inorganic Chemistry Communications (2025): 115665.

[114] Huong, Vu Hoang, et al. "Unveiling the synergistic interplay of appropriate oxygen vacancies and S-scheme heterojunction structures in OVs-TiO2/g-C3N4 catalyst for efficient RhB photodegradation and H2 production." Journal of Alloys and Compounds 972 (2024): 172722.

[115] Zhao, Sheng-Zhe, et al. "Direct Z-scheme g-C3N4/TiO2 heterojunction porous nanotubes: An ingenious synthesis strategy to enhance photocatalytic activity." Journal of Environmental Chemical Engineering 11.2 (2023): 109366.

[116] Alsalme, Ali, et al. "Fabrication of S-scheme TiO2/g-C3N4 nanocomposites for generation of hydrogen gas and removal of fluorescein dye." Diamond and related materials 122 (2022): 108819.

[117] Hu, Chechia, et al. "Type-II heterojunction of g-C3N4/TiO2 hollow spheres for photocatalytic H2 production and degradation of organic contaminants in water." Journal of Alloys and Compounds 1032 (2025): 181104.

[118] Yang, Songyu, et al. "Enhanced photocatalytic hydrogen production of S-scheme TiO2/g-C3N4 heterojunction loaded with single-atom Ni." Journal of Materials Science & Technology 175 (2024): 104-114.

[119] Sahar, Kashaf Ul, et al. "Coupling plasmonic and electron-mediated effects in Ag x@ r--TiO 2/gC 3 N 4 heterostructures for enhanced catalytic hydrogen generation." Nanoscale Advances 7.17 (2025): 5384-5400.

[120] Xu, Shuchang, et al. "Ultrafast plasma method allows rapid immobilization of monatomic copper on carboxyl-deficient g-C3N4 for efficient photocatalytic hydrogen production." Frontiers in Chemistry 10 (2022): 972496.

[121] Ong, Wee-Jun, et al. "Graphitic carbon nitride (g-C3N4)-based photocatalysts for artificial photosynthesis and environmental remediation: are we a step closer to achieving sustainability?." Chemical reviews 116.12 (2016): 7159-7329.

[122] Wang, Huanli, et al. "Semiconductor heterojunction photocatalysts: design, construction, and photocatalytic performances." Chemical Society Reviews 43.15 (2014): 5234-5244.

[123] Chen, Xiaobo, et al. "Nanomaterials for renewable energy production and storage." Chemical Society Reviews 41.23 (2012): 7909-7937.

[124] Zhu, Bicheng, et al. "Construction of 2D S-scheme heterojunction photocatalyst." Advanced Materials 36.8 (2024): 2310600.

[125] Kudo, Akihiko, and Yugo Miseki. "Heterogeneous photocatalyst materials for water splitting." Chemical Society Reviews 38.1 (2009): 253-278.

[126] P A, Mathina. "Nanomaterials for Energy Harvesting and Storage in Nano-Ecosystems." Nano-Ecosystems. Springer, Singapore, 2026. 67-88.

[127] Vasu, Dhanapal, et al. "Integrating DFT Insights and Photocatalytic Performance of Halogen-Doped Graphitic Carbon Nitride for Sustainable Wastewater Remediation." Synthetic Metals (2026): 118084.

[128] Wu, Xinhe, et al. "COF-based S-scheme heterojunction photocatalyst." Advanced Materials 38.2 (2026): e11322.

[129] Ren, Haitao, et al. "Coordination engineering in dual S-scheme heterojunction for photocatalytic applications: Research progress, key challenges and future horizons." Coordination Chemistry Reviews 548 (2026): 217183.

[130] Garg, Devesh, et al. "Vapor-Phase Synthesis of Potassium-Doped Polymeric Carbon Nitride Photocatalytic Panels." Small (2026): e13234.

[131] Chen, Qingsong, et al. "Construction of S-type heterostructure Er2O3/g-C3N4 for enhanced photocatalytic CO2 reduction performance." Optical and Quantum Electronics 58.3 (2026): 114.[132] Zhao, Yang, et al. "Construction of porous sheet-like g-C_3N_4/CdS hierarchical heterojunctions and their application in photocatalytic hydrogen production." Applied Materials Today 49 (2026): 103130.

[133] Low, Jingxiang, et al. "Heterojunction photocatalysts." Advanced materials 29.20 (2017): 1601694.

[134] Zhu, Bicheng, et al. "Construction of 2D S-scheme heterojunction photocatalyst." Advanced Materials 36.8 (2024): 2310600.